Boundary-Layer Meteorology
https://doi.org/10.1007/s10546-022-00729-2

RESEARCH ARTICLE

Uncrewed Aircraft System Measurements of Atmospheric Surface-Layer Structure During Morning Transition

Loiy Al-Ghussain[1] · **Sean C. C. Bailey**[1]

Received: 25 October 2021 / Accepted: 24 June 2022

Abstract
This study applies uncrewed aircraft systems towards the investigation of surface-layer structure during the morning transition. Three uncrewed aircraft systems simultaneously measuring horizontal transects were partnered with a fourth measuring vertical profiles during two consecutive mornings as part of the 2017 Collaboration Leading Operational Unmanned Aerial System Development for Meteorology and Atmospheric Physics (CLOUDMAP) measurement campaign near Stillwater, Oklahoma, USA. Data were analyzed to extract time-dependent single-point statistics of kinematic and thermodynamic variables from the uncrewed aircraft systems. In addition, an approach is presented by which multi-point spatial statistics in the form of auto- and cross-correlations could be calculated from the measurements. The results reflect differences in the evolution of spatial statistics with altitude for each of the two days at scales smaller than 500 m, despite very similar synoptic conditions. Conditional averaging was also applied to identify the structure of sweep and ejection motions and results revealed similarities to observations from canonical wall-bounded flow.

Keywords Coherent structures · Morning transition · Uncrewed aircraft systems · Surface layer

1 Introduction

The atmospheric surface layer—the lowest 10% of the atmospheric boundary layer—impacts the dynamics of the atmosphere as it is the region of exchange between the Earth's surface and the atmosphere of mass, heat, and momentum as well as the transport of anthropogenic and natural chemical constituents (e.g., Monin and Obukhov 1959; Garratt 1994; Liu and Liang 2010; Su et al. 2020). Much of this exchange is through turbulent transport. Furthermore, a significant contribution to turbulent transport is carried out through large-scale turbulent motions referred to as coherent structures (e.g., Brown and Roshko 1974; Gao et al. 1989; Robinson 1991; Lu and Fitzjarrald 1994; Huang et al. 2009; Marusic et al. 2010; Park et al. 2016). As noted by Wyngaard (2010), coherent structures also play an important role in

✉ Sean C. C. Bailey
sean.bailey@uky.edu

[1] Department of Mechanical and Aerospace Engineering, University of Kentucky, Lexington, KY 40506, USA

the inertial cascade process. These structures act as an intermediary in the extraction of kinetic energy from the mean flow, which is then transferred to smaller scales in the form of increasingly isotropic motions.

Investigation of the coherent structures that populate in canonical smooth-walled, neutrally stable, zero-pressure-gradient turbulent boundary layers have connected coherent structures to sweeping and ejection motions responsible for turbulence production and transport (Willmarth and Lu 1972; Blackwelder and Kaplan 1976; Robinson 1991). Recent studies have also revealed that these sweeps and ejections are part of a hierarchy of coherent structures (Adrian 2007; Jiménez 2011) including: sublayer streaks (Kline et al. 1967); hairpin vortices (Head and Bandyopadhyay 1981); large-scale motions (LSMs) (Kim and Adrian 1999; Guala et al. 2006; Balakumar and Adrian 2007) attributed to self-organization of hairpin vortices into packets (Adrian et al. 2000; Ganapathisubramani et al. 2003; Tomkins and Adrian 2003; Hutchins et al. 2005) and very-large-scale motions (VLSMs) or superstructures (Kim and Adrian 1999; Tomkins and Adrian 2005; Guala et al. 2006; Balakumar and Adrian 2007; Hutchins and Marusic 2007; Monty et al. 2007, 2009). Spectral analysis of LSMs and VLSMs in canonical smooth-walled, wall-bounded turbulence indicates that they make a non-negligible contribution to turbulence kinetic energy and Reynolds stress production (Guala et al. 2006; Balakumar and Adrian 2007), which distinguishes them from the inactive motions proposed by Townsend (1976).

Coherent structures have also been clearly identified in the atmospheric surface layer and boundary layer, particularly through the use of arrays of sonic and cup anemometers (Segalini and Alfredsson 2012), sonic detection and ranging (sodar), light detection and ranging (lidar) (Froidevaux et al. 2012), large-eddy simulations (LESs) (Inagaki et al. 2012) and particle image velocimetry in controlled situations (Takimoto et al. 2011). Coherent structures in the form of near-surface organized eddies with anisotropic turbulence characteristics are frequently observed (Drobinski et al. 2004) and verified as characteristic of the large-scale turbulence in the atmospheric boundary layer (Paw et al. 1992; Boppe et al. 1999; Krunsche and de Oliveira 2004). These coherent structures, although poorly defined, have been cited as being responsible for up to 75% of the turbulent fluxes in the atmospheric surface layer (Gao et al. 1989), although a wide range of values have also been cited including, 40% (Lu and Fitzjarrald 1994), 60% (Drobinski et al. 2004), 30% (Feigenwinter and Vogt 2005) and 30–70% (Barthlott et al. 2007).

Evidence suggests that the hierarchy of structures in the atmosphere could contain some of the same elements as that of canonical wall flows, including low-speed streaks and superstructures (e.g., Träumner et al. 2015; Lotfy et al. 2019) and persistent flow features in humidity patterns consistent with LSMs (Froidevaux et al. 2012). Low-speed streaks have also been found to form under neutral, slightly stable, and unstable conditions (e.g., Etling and Brown 1993; Moeng and Sullivan 1994; Kim and Park 2003). In the atmospheric boundary layer the streaks are described as organized regions of low momentum stretched in the streamwise direction with streamwise length of 500 m to 2000 m and spanwise width of 100 m to 200 m (e.g., Moeng and Sullivan 1994; Kim and Park 2003; Newsom et al. 2008; Iwai et al. 2008; Alcayaga et al. 2020). These low-momentum regions have been connected to LSMs and VLSMs (Thomas and Foken 2007; Horiguchi et al. 2012; Eder et al. 2013; Dias Júnior et al. 2013) with LSMs having time scales on the order of 15 s to 40 s whereas VLSMs have time scales between 60 s and 140 s. There is also an indication that boundary-layer stability can alter the organization of coherent structures. Under neutral conditions the inclination angle of these structures (in the streamwise–wall-normal plane) has been measured to be 12°, whereas this angle has been observed to be 15° under stable conditions

and between 10° to 56° under convective conditions (Chauhan et al. 2013; Lotfy and Harun 2018; Salesky and Anderson 2018; Lotfy et al. 2019).

In addition, the atmospheric boundary layer has also been found to contain additional large coherent motions in the form of convective rolls on the order of several kilometres (e.g.,Kelly 1982; Etling and Brown 1993; Weckwerth et al. 1997; Drobinski et al. 1998; Weckwerth et al. 1999; Salesky et al. 2017; Chow et al. 2019). These structures are developed in the presence of buoyant and shear production under moderate convective conditions and high Reynolds numbers (Sikma et al. 2018).

Within the atmospheric surface layer, such turbulence structure is typically inferred from stationary (in situ) measurement systems. However, this typically requires the spatial distribution of wind to be inferred using Taylor's frozen-flow hypothesis, which is poorly realized at large scales, particularly within non-stationary flow and subject to the diurnal stability cycle (Metzger and Holmes 2008). This shortcoming is usually overcome by using multiple synchronous measurement systems at different locations (Ingenhorst et al. 2021). For instance, studies examining coherent structures have employed multiple sonic anemometers (Sadani and Kulkarni 2001; Barthlott et al. 2007; Liu et al. 2019; Gu et al. 2019; Lotfy et al. 2019), Doppler-lidar systems (Träumner et al. 2015; Alcayaga et al. 2020), and hotwire probes (Lotfy and Harun 2018). Large-eddy simulation has also been increasingly applied to the study of atmospheric-boundary-layer turbulence, but due to its high Reynolds numbers, LES cannot resolve the near-wall eddies and frequently relies on wall models. However, as noted by Senocak et al. (2007), such models can alter the arrangement of large-scale coherent structures.

Conversely, uncrewed aircraft systems (UASs), or remotely piloted aircraft systems, are increasingly being employed in atmospheric research. Uncrewed aircraft systems have the ability to traverse through the flow spatially over time scales faster than those of the coherent structures, allowing for a snapshot of the turbulence structure along the flight path. In addition, due to their lower cruising speed (between 10 m s^{-1} and 30 m s^{-1}) compared with crewed aircraft (between 50 m s^{-1} and 200 m s^{-1}), UASs have the ability to acquire measurements with higher spatial resolution with the same sampling rate (Bärfuss et al. 2018; Zhou et al. 2018; Barbieri et al. 2019). Hence, UASs have been utilized extensively in atmospheric research to sample thermodynamic and kinematic variables (Egger et al. 2002; Hobbs et al. 2002; Balsley et al. 2013; Witte et al. 2017; Rautenberg et al. 2018; Bärfuss et al. 2018; Jacob et al. 2018; Barbieri et al. 2019; Bailey et al. 2019). One trade-off in the use of UASs is that their deployment is a labour-intensive process. Hence, they are typically only deployed over limited observation periods (Witte et al. 2017; Bärfuss et al. 2018; Jacob et al. 2018; Barbieri et al. 2019; González-Rocha et al. 2020).

There have been relatively few concerted UAS deployments investigating the morning transition process (Bange et al. 2007; Bennett et al. 2010; Wildmann et al. 2015; Higgins et al. 2018) and none of these studies (to the best of our knowledge) has investigated the characteristics of the coherent structures in the surface boundary layer during the morning transition. This paper, therefore, presents the results from four UAS simultaneously measuring the boundary-layer characteristics over the morning transition during a limited field deployment. Particular attention is paid to the demonstration of UASs capability to resolve the structure and evolution of coherent structures which form during the morning transition.

The remainder of the manuscript is divided into three main sections; Sect. 2 summarizes information regrading the location of the study with some topographic information in addition to details about the UASs and other measurement devices used in this study. Afterwards, Sect. 3 presents the main findings and their interpretation starting with the boundary-layer stability in Sect. 3.1 then moving to the discussion of the surface-layer properties in Sect.

3.2. Section 3.3 presents the visualization and related discussion of the temperature and velocity fluctuation fields, Sect. 3.4 presents the results and the discussion of a methodology to determine spatio–temporal correlations of the velocity and temperature fields, and Sect. 3.5 analyzes the structure and contribution of coherent structures within the framework of sweep and ejection events. Finally, a summary and discussion of the main findings and conclusions are presented in Sect. 4.

2 Overview of Measurements

The measurements presented here were collected on 27 and 28 June 2017, referred to as Case 1 and Case 2, respectively. These observations were conducted as part of the Collaboration Leading Operational Unmanned Aerial System Development for Meteorology and Atmospheric Physics (CLOUDMAP) 2017 field campaign (Jacob et al. 2018) performed at the Oklahoma State University's unmanned aircraft flight station (UAFS) near Stillwater, Oklahoma (located at 36.162785° latitude, −96.8366762° longitude, and 288 m above sea level). Here, we will use local time (LT) when referencing the time of day, which was central daylight time (CDT) or UTC – 5. For the cases being considered, sunrise was at 0613 LT with nautical twilight beginning at 0505 LT and civil twilight at 0543 LT.

2.1 Overview of Topography

The measurement site is surrounded by gently rolling hills interspersed by creeks corresponding to approximately 30 m of elevation change over 1000 m horizontal distance (Fig. 1a). The surrounding land use is primarily agricultural cattle pasture with intermittent stands of trees. An approximately 2-km^2 stand of trees is located 300 m to the north-east of the UAFS (Fig. 1b), with a second equivalently sized stand approximately 1 km to the south.

2.2 Measurement Systems

The primary measurement systems used for this study consisted of three fixed-wing UAS, used to conduct horizontal transects, with a fourth rotorcraft used to conduct vertical profiling. A sonic anemometer mounted on a 7-m tower along with three cup-and-vane anemometers and pressure, temperature, and humidity sensors was collocated with the vertical profiling site. The heights of the sonic anemometer and the three cup-and-vane anemometers were 8.2 m, 5.6 m, 4.5 m, and 3.4 m, respectively.

The three fixed-wing UASs were BLUECAT5 aircraft (for details see Witte et al. 2017; Bailey et al. 2019; Al-Ghussain and Bailey 2021) flown simultaneously at three different heights, as illustrated in Fig. 1c. Each flight consisted of repeatedly traversing the same 1000 m long straight line transect at true air speed of 18 m s^{-1} and at constant altitude above sea level, resulting in approximately 15 m variability in aircraft above ground level (a.g.l.) as indicated in Fig. 1. Typically 40 to 50 transects were made per flight in alternating directions with each transect taking around 75 s. Measurements typically consisted of all three aircraft being flown for approximately 40 min of flight time, after which the aircraft were recovered, data downloaded, and batteries changed. Five flights were conducted for both Case 1 and Case 2, with Case 1 initiating measurements just after nautical sunrise at 0600 LT and measuring nearly continuously to 1130 LT with a fifth flight conducted at 1330 LT. Case 2 initiated measurements at 0600 LT with all five flights conducted before 1200 LT. For Case 1,

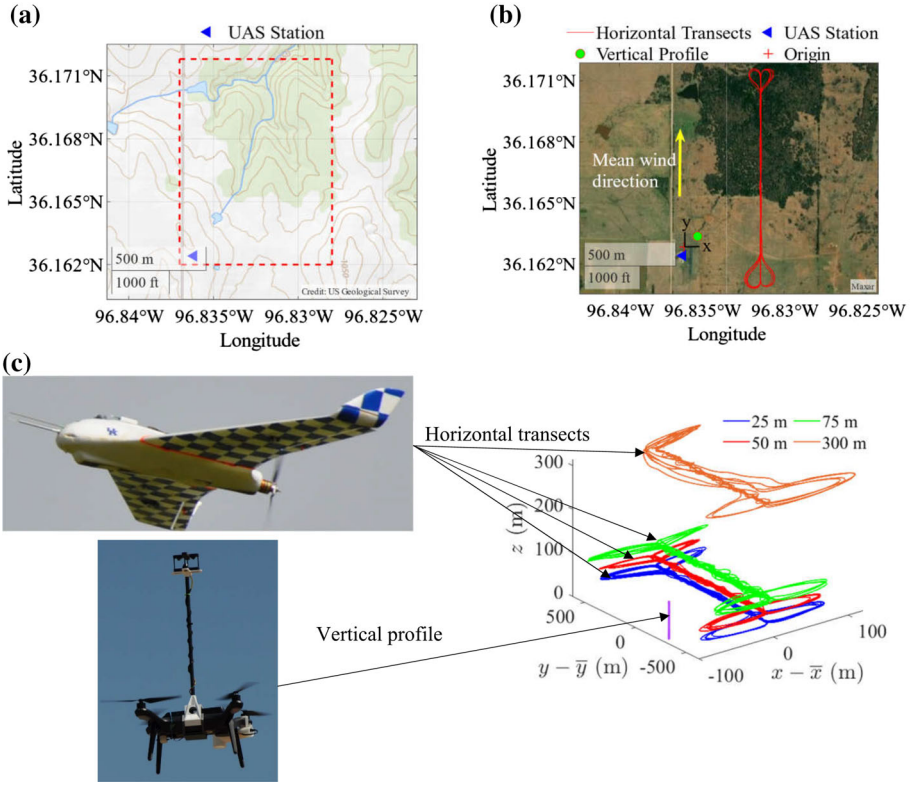

Fig. 1 **a** Topographic map showing terrain surrounding measurement with **b** detailed satellite photograph of area highlighted by red box in (**a**). **c** Shows the fixed-wing and rotorcraft UAS used, along with an additional illustration of the different flight path altitudes. Approximate location of flight trajectories and of fixed-wing UAS and measurement location of the rotocraft indicated by red line and green dot respectively in (**b**). Contour lines in (**a**) correspond to 3.048 m elevation separation

the three aircraft were flown at nominal altitudes of 25 m, 50 m, and 75 m a.g.l. relative to takeoff ground level, whereas for Case 2, intermittent aircraft problems resulted in only the 50 m a.g.l. height being measured continuously, with additional measurements conducted at 25 m, 75 m, and 300 m depending on aircraft availability.

The rotorcraft used was a 3DR SOLO aircraft (for details see Bailey et al. 2019) illustrated in Fig. 1c. The aircraft was flown simultaneously with the fixed wing aircraft and consisted of vertical ascents and descents at 2 m s^{-1} between 10 m and 100 m. Up to 10 ascent/descent combinations were flown in a single flight before the aircraft's batteries required changing. Once the batteries were changed, the aircraft was returned to flight. Due to a shorter endurance, approximately four flights of the rotorcraft were conducted for each fixed-wing flight with times between flights depending on battery availability and charge rates. However, most flights were separated by less than 5 min.

Each aircraft was equipped with an iMet-XQ (InterMET Inc., Grand Rapids, Michigan, U.S.A.) capable of logging temperature (T), pressure (p), and relative humidity (RH) at a frequency of 1 Hz. The fixed-wing aircraft measured three components of wind using a custom-built five-hole-probe logged at 200 Hz, but, due to viscous damping within the sensor tubing, was only capable of measuring frequency content lower than 60 Hz. To measure the

winds, the rotorcraft was equipped with a Trisonica Mini three-dimensional sonic anemometer (Anemoment LLC, Longmont, Colorado, U.S.A.) mounted on a 0.38 m mast to prevent distortion of the measured wind by the aircraft's rotor wash. Although nominally it is a three-component anemometer, when operated in the configuration used here, only the horizontal components of wind are considered reliable. Additional details about the aircraft, sensing systems and data reduction procedures can be found in Witte et al. (2017) and Bailey et al. (2019) with an intercomparison and evaluation of system accuracy provided in Barbieri et al. (2019).

The measured quantities are presented in an (x, y, z) coordinate system with the x-axis directed towards the east, the y-axis directed towards the north, and the z-axis directed up, and with the origin of the coordinate system located at the aircraft launch point (Fig. 1b). The wind velocity components (u, v, w) are aligned with the (x, y, z) axes, respectively.

2.3 Weather Conditions During Observation Periods

During 27 and 28 June 2017, Oklahoma was under the influence of return flow on the back side of surface high pressure centred over the east coast, which likely resulted in a strong south-south-westerly low-level jet over most of Oklahoma. A dryline and weak frontal boundary developed over the Oklahoma panhandle extending into Texas by the second day of operations.

Meteorological conditions reported at the nearby Stillwater airport (KSWO) for 27 June 2017 indicate a recorded overnight low temperature of 19 °C at 0553 LT and a recorded daytime high of 34 °C at 1553 LT. Relative humidity peaked at 81.3% at the same time in the morning and reached a value of 41.2% when the temperature reached its maximum. During the observation period, surface winds were reported as initially being from 140° at 2.6 m s^{-1} shifting to between 160° and 180° after 0650 LT and increasing in magnitude to 5.7 m s^{-1} by the end of the observation period. Clear-sky conditions were reported until 1100 LT, at which point, few and then scattered clouds were observed at 945 m a.g.l.

On 28 June 2017, the receding high pressure system continued to reduce surface pressure, with a recorded overnight low temperature of 23 °C at 0553 LT and a recorded daytime high of 34 °C at 1653 LT. Similar moisture content was present with a peak relative humidity of 81.2% measured in the morning, reaching a low value of 37.4% observed at 1653 LT. Surface winds continued to be southerly, with reported direction of 170° to 190°, but with much higher magnitude than the first day, increasing from 5.7 m s^{-1} to 8.2 m s^{-1} by the end of the measurements. Skies were reported as clear for the majority of the morning, with a few clouds observed between 1000 LT and 1200 LT at 1200 m a.g.l.

3 Results and Discussion

3.1 Stability Conditions

To assess the surface-layer stability during the period of observation, the flux Richardson number

$$Ri = \frac{\frac{g}{\overline{T}_v}\overline{w'\theta'_v}}{-u_\tau^3 \frac{\partial \overline{U}}{\partial z}} \tag{1}$$

was calculated from the sonic anemometer tower measurements. Here, g is the acceleration due to gravity, and we use Reynolds averaging, e.g., $u(t) = \overline{u} + u'(t)$ where the overline

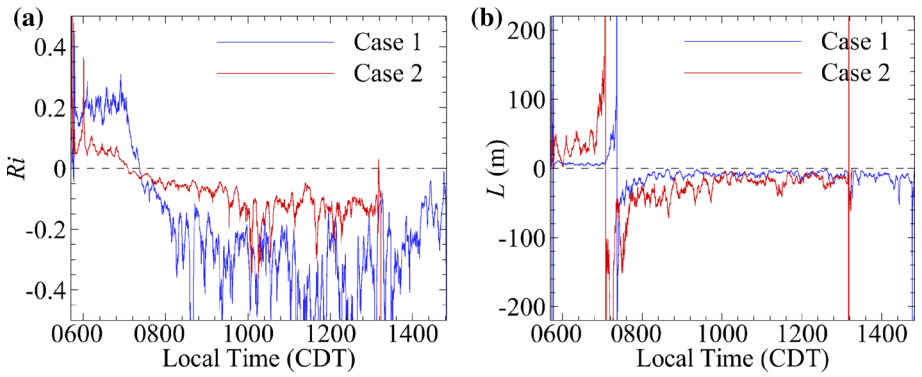

Fig. 2 **a** Ri and **b** L calculated from the 7-m tower data for the duration of Case 1 and Case 2 observation periods

indicates a 5-min moving time average. Furthermore, virtual temperature is approximated as $T_v = T(1 + 0.61r_v)$, where r_v is the vapour mixing ratio and the virtual potential temperature is calculated from $\theta_v = T_v(100 \times 10^3/\overline{p})^{0.286}$. Moreover, the friction velocity was approximated using $u_\tau = (\overline{u'w'}^2 + \overline{v'w'}^2)^{1/4}$, where u' v' are the horizontal and w' the vertical velocity components, and the wind speed from $U = (u^2 + v^2)^{1/2}$. Finally, the velocity gradient was estimated by averaging the gradients measured between the cup and vane anemometers and sonic anemometer located on the tower. To minimize uncertainty caused by precision errors in the instruments propagating via the small separation between vertical measurement points, several approaches were evaluated. It was found that the approach that best minimized the impact of sensor precision error on the gradient calculations was to calculate the linear gradients between the different combinations of measurement heights of the cup and vane anemometers and sonic anemometer and average the result.

The resulting time evolution of Ri is presented in Fig. 2a. The figure shows slightly different behaviour for Case 1 than Case 2 with the results indicating more stable conditions existed for Case 1 than Case 2, although neither larger than the suggested critical Richardson number of 0.25 (Grachev et al. 2013). Hence, both cases can be considered as dynamically unstable and prone to turbulence production. Figure 2a also indicates that the boundary layer transitioned to convective conditions slightly earlier for Case 2 than for Case 1, becoming negative at approximately 0720 LT whereas this transition occurred at 0740 LT for Case 1.

The corresponding Obukhov length scale (e.g., Leelőssy et al. 2014)

$$L = \frac{-u_\tau^3 \overline{T}_v}{\kappa g \overline{w'\theta_v'}} \tag{2}$$

is presented in Fig. 2b, where κ is the von Kármán constant. The results reflect the difference in Ri, with Case 2 showing a $|L| \approx 35$ m prior to transition, whereas Case 1 indicates $|L| \approx 5$ m for the same period. Following transition, for Case 1 $|L| \approx 10$ m whereas for Case 2 $|L| \approx 50$ m until 1000 LT, approaching $|L| \approx 10$ m for the latter portions of the morning.

3.2 Mean Properties of the Surface Layer

The difference between the values of the stability parameters for each case is reflected in the atmospheric properties measured at the UAS flight altitudes. To calculate statistics from the

fixed-wing UAS, we considered only the portion of the flight when the UAS were in their automated flight pattern. As each flight consisted of several straight line transects, we then treated each transect as an individual sample. By assuming each transect occurs under steady state conditions, the averaged quantities are then spatially averaged over a nominal distance of 1000 m and with averages over individual transects indicated by $\langle\rangle$ brackets.

Figure 3a, b show the evolution of $\langle\theta_v\rangle$ measured by the fixed-wing UAS for Case 1 (Fig. 3a) and Case 2 (Fig. 3b). The corresponding values of wind components $\langle u\rangle$ and and $\langle v\rangle$ are shown in Fig. 3c, d. These panels show that the winds were generally from the south (positive v) for both cases with an increase in virtual potential air temperature at all measured altitudes after the inversion of Ri occurs. For Case 1 (Fig. 3a, c) there are measurable vertical gradients in both wind velocity and $\langle\theta_v\rangle$ prior to 0900 LT, with approximately uniform conditions measured after this time. Conversely, for Case 2, strong gradients are only evident in the mean wind velocity, whereas the $\langle\theta_v\rangle$ remains relatively homogeneous for all heights during the period of measurement.

These differences can be explained by the proportionate differences in stability conditions between the two cases. Figure 3e, f show the turbulence kinetic energy for Case 1 and Case 2, respectively, calculated using

$$\langle k\rangle = \frac{1}{2}\left(\langle u'^2\rangle + \langle v'^2\rangle + \langle w'^2\rangle\right). \tag{3}$$

Comparison of the two cases shows higher magnitude of $\langle k\rangle$ for Case 2 during the period of positive Ri, reflecting an increase in mechanical production of turbulence. Notably, both cases show higher values of $\langle k\rangle$ near the surface for this period as well. As the morning progresses, the general trend was for $\langle k\rangle$ to increase, with Case 2 continuing to show higher magnitudes, but with both cases also showing increasing variability in $\langle k\rangle$. The latter behaviour suggests two interpretations: increasing contribution to turbulence kinetic energy from spatial scales larger than 1000 m (e.g., larger than that of a representative thermal which usually has a radius of less than 600 m, (Romps and Charn 2015; Hernandez-Deckers and Sherwood 2016); or horizontal advection of turbulent air from other locations. Neither of these explanations are mutually exclusive, as large-scale coherent motions would be expected to advect turbulence and other atmospheric properties over commensurate spatial scales (Willmarth and Lu 1972; Blackwelder and Kaplan 1976; Robinson 1991).

A Similar behaviour is observed for $\langle\theta_v'^2\rangle$, which describes the temperature and density fluctuations in the atmospheric surface layer and is shown in Fig. 3g, h for Case 1 and Case 2, respectively. These results show an increase in the temperature fluctuations for both cases, but with Case 1 showing an earlier and larger increase. Both cases exhibited unsteadiness in $\langle\theta_v'^2\rangle$ having the same time scale (nominally one hour) as observed for the unsteadiness in $\langle k\rangle$.

Greater insight into the source of these fluctuations could be found by examination of the temporal evolution of the turbulence kinetic energy budget terms for both cases. Note that it was found that the sample rate of p, T and RH varied around the 1-Hz nominal frequency throughout the flight, and therefore it was not possible to accurately align (u, v, w) and T in time (as they were logged separately and aligned in post-processing). This prohibited the calculation of $\langle w'\theta_v'\rangle$ at length scales smaller than approximately 20 m and, in turn, provide accurate estimation of the buoyant production. However, an estimate of mechanical production can be made using

$$\langle P\rangle = \left(\langle u'w'\rangle^2 + \langle v'w'\rangle^2\right)^{1/2}\frac{\partial\overline{U}}{\partial z}, \tag{4}$$

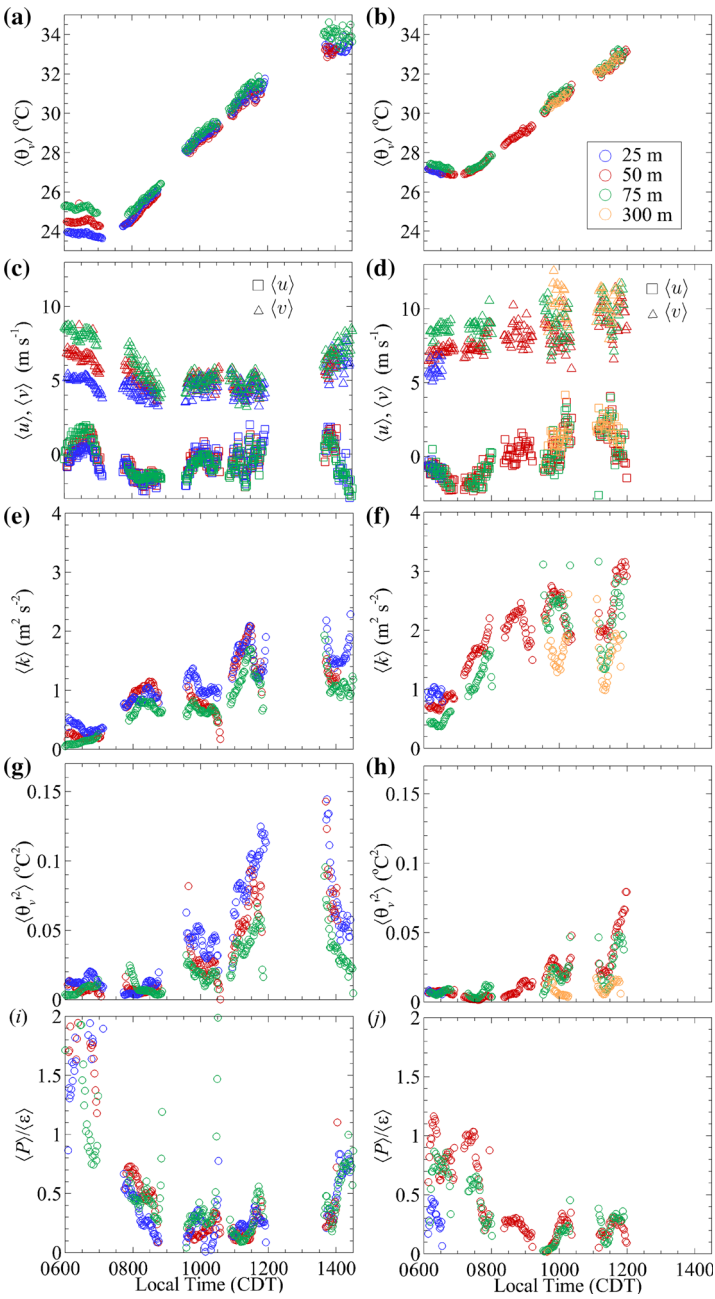

Fig. 3 Time-dependence of: **a** $\langle\theta_v\rangle$ for Case 1; **b** $\langle\theta_v\rangle$ for Case 2; **c** $\langle u\rangle$ and $\langle v\rangle$ for Case 1; **d** $\langle u\rangle$ and $\langle v\rangle$ for Case 2; **e** $\langle k\rangle$ for Case 1; **f** $\langle k\rangle$ for Case 2; **g** $\langle\theta_v'^2\rangle$ for Case 1; **h** $\langle\theta_v'^2\rangle$ for Case 2; **i** $\langle P\rangle/\langle\varepsilon\rangle$ for Case 1; and **j** $\langle P\rangle/\langle\varepsilon\rangle$ for Case 2. Blue symbols indicate measurements made at $z = 25$ m, red symbols indicate measurements made at $z = 50$ m, green symbols indicate measurements made at $z = 75$ m, and orange symbols indicate measurements made at $z = 300$ m

by assuming negligible horizontal gradients in $\overline{U}$. Note that due to the scatter in the $\langle u \rangle$ and $\langle v \rangle$ results, the gradient of $\overline{U}$ was calculated from the rotorcraft measurements during each 10 min flight. This was done by first averaging the measured value of U over 5-min intervals and then fitting the curve $\overline{U} = A \log(z)^2 + B \log(z) + C$ to the resulting profile, where A, B, and C are constants, thus producing smooth estimates of $\partial \overline{U}/\partial z$. In addition, an estimate of the dissipation rate, $\langle \varepsilon \rangle$, was made from the wavenumber spectrum, $\Phi(2\pi/\lambda)$, measured for each transect, where λ is wavelength. To do so, the mean dissipation rate for each transect was calculated from the spectrum using

$$\langle \varepsilon \rangle = \left(\frac{\Phi}{0.49(2\pi/\lambda)^{-5/3}} \right)^{3/2}. \tag{5}$$

Details of this calculation procedure can be found in Bailey et al. (2019).

The resulting time-dependent ratio $\langle P \rangle / \langle \varepsilon \rangle$ is presented in Fig. 3i, j for Case 1 and Case 2. If, for the sake of simplicity, one assumes negligible turbulence advection, that $\partial \langle k \rangle / \partial t \approx 0$ (i.e., the turbulence kinetic energy is quasi-stationary, Nilsson et al. 2016) and that pressure fluctuations can be neglected, it is possible to interpret Fig. 3i, j as an estimate of the relative contribution of mechanical production to total production. Note that these assumptions are not likely to be completely satisfied, however, as reflected in the strong time-dependence of Fig. 3e, f. Both cases show mechanical production equating or exceeding dissipation at the start of the observation period, with Case 1 indicating mechanical production exceeding dissipation near the surface due to low measured dissipation rates. For the remainder of the observation period, however, the trend in $\langle P \rangle / \langle \varepsilon \rangle$ is very similar for both cases. Notably, the mechanical production remains the primary means of turbulent production until about 0830 LT.

3.3 Visualization of Flow Structure

Having established the background statistical description of the surface-layer properties, in this section we examine the large-scale structure of the turbulence as revealed through the fluctuation fields $\theta_v'(t, x, y, z)$ and $U'(t, x, y, z)$. We first look at the time–height plots of $\theta_v'(t, z) = \theta_v(t, z) - \langle \theta_v(t, z) \rangle$ where θ_v is the virtual potential temperature measured by the rotorcraft and $\langle\ \rangle$ in this context is used to indicate an average in both t and z, with the time averaging being applied over the duration of each 10 min flight.

Isocontours of $\theta_v'(t, z)$ are presented in Fig. 4a, b for Case 1 and Fig. 4c, d for Case 2. These isocontours reveal strong vertical stratification of θ_v before 0800 LT for Case 1, reflecting the stable conditions observed in Fig. 2. As the morning progresses, the stratification decays, with moderate temperature variability observed from 0800 LT to 0900 LT. After 0900 LT, the θ_v' perturbations organize into intermittent, vertically oriented structures. These structures have varying time scales roughly on the order of 2 min and, assuming advection velocity of 5 m s^{-1} (Fig. 3c) are consistent with turbulent thermals having horizontal length scales on the order of 500 m. Similar behaviour is observed for Case 2, shown in Fig. 4c, d, except that the stable stratification in the early morning hours is weaker and consequently more unsteadiness can be observed in the temperature field. Once convective conditions develop after 0930 LT, the behaviour is very similar to that of Case 1.

As could be expected, isocontours of $U'(t, z)$, presented in Fig. 5a, b for Case 1 and Fig. 5c, d for Case 2, demonstrated virtually identical time-dependence as that of $\theta_v'(t, z)$. Although a clear velocity gradient is evident for Case 1 prior to 0830 LT, due to the reduced thermal stratification for Case 2 the velocity perturbations show increased variability in both time

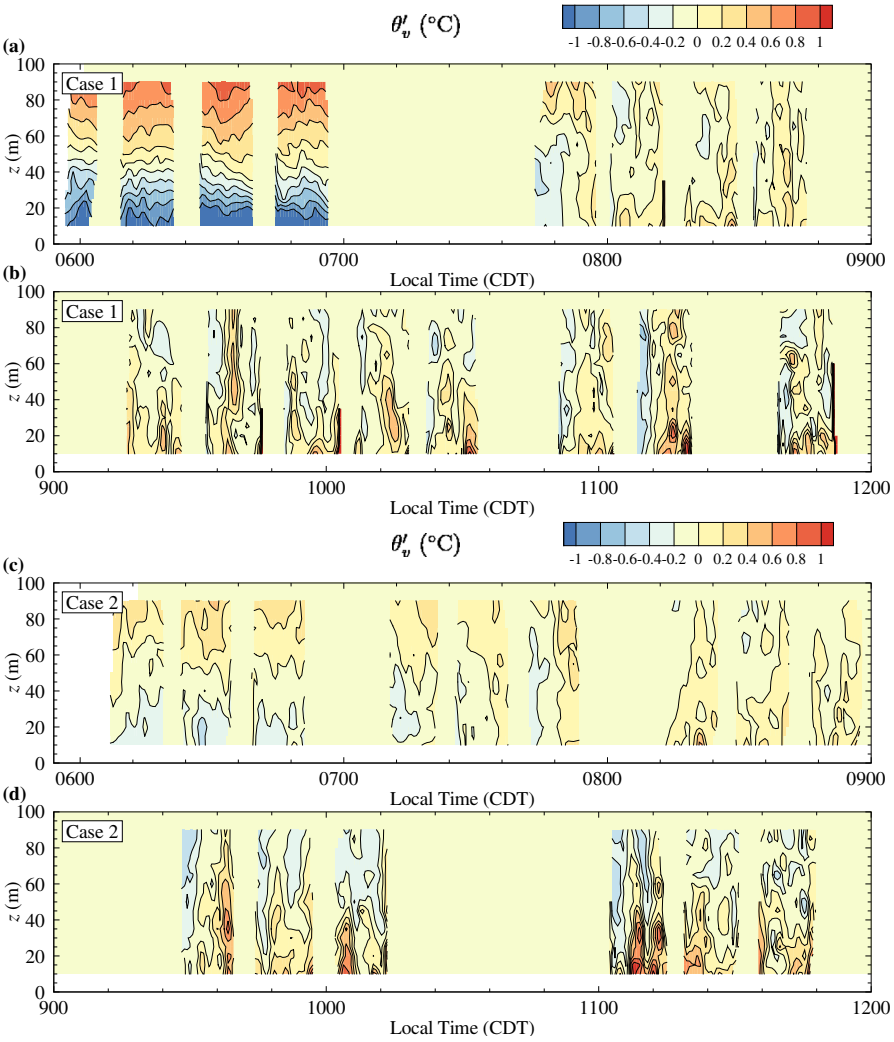

Fig. 4 Isocontours of $\theta_v'(t, z)$ measured by rotorcraft UAS for: **a** 0600 LT to 0900 LT and **b** 0900 LT to 1200 LT for Case 1 and **c** 0600 LT to 0900 LT and **d** 0900 LT to 1200 LT for Case 2

and space, reflected in the differences in $\langle k \rangle$ between the two cases as observed in Fig. 3e, f. Once the thermals develop, a qualitative observation can be made that the negative velocity perturbations are coincident with positive temperature perturbations and vice versa, providing confidence that the contours in Figs. 4 and 5 are visualizations of large-scale mixing events.

Similar visualizations can be produced from the fixed-wing UAS measurements. However, for these flights the visualizations are in the form of isocontours of $\theta_v'(t, y)$ and $U'(t, y)$ which are provided in Fig. 6 for $z = 50$ m for Case 1. As shown in Fig. 6a, b, the fluctuations in θ_v' and U' are initially above the mean value for $y > 500$ m and below the mean value for $y < 500$ m prior to 0700 LT. This behaviour is consistent with topographically induced internal layer formation as it is similar to the observations made from field experiments (Gao et al. 1989; Lu and Fitzjarrald 1994; Alcayaga et al. 2020) and LES (Perret and Patton

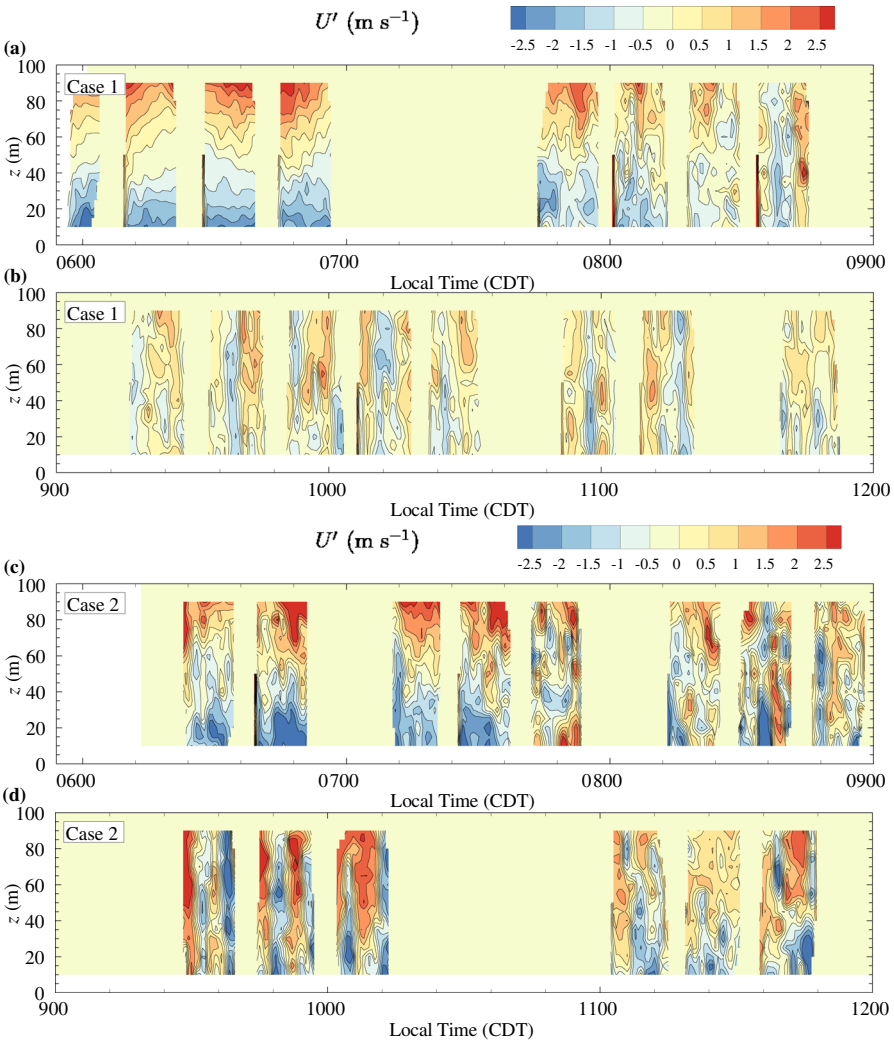

Fig. 5 Isocontours of $U'(t, z)$ measured by rotorcraft UAS for: **a** 0600 LT to 0900 LT and **b** 0900 LT to 1200 LT for Case 1 and **c** 0600 LT to 0900 LT and **d** 0900 LT to 1200 LT for Case 2

2021) studies examining the effect of forest and vegetation on the flow field. Note also that the aircraft was flying over a transition from pasture to trees for $y \gtrsim 300$ m (Fig. 1b), producing a likely source of local perturbation from the mean flow. After 0800 LT, the fluctuations appear more stochastic, taking the form of increasingly smaller-scale motions with the convective conditions after 1000 LT characterized by motions having length scales on the order of $y \approx 300$ m. The same organization appears in both temperature and velocity perturbations and is consistent with the formation of turbulent thermals observed in Figs. 4 and 5. For Case 2, which had higher values of $\langle k \rangle$ and lower stability in the early morning, the positive Ri period is characterized by large-scale perturbations, on the order of $y \approx 500$ m, which break into smaller scale thermal-associated events after inversion of Ri.

3.4 Velocity and Temperature Correlations

Of particular interest in Fig. 6, is qualitative evidence of organization over long time periods (nominally 20 min), suggesting structural organization at time scales longer than each transect. To educe these motions, velocity and temperature correlations were conducted noting that the existence of non-zero trends in the autocorrelation indicates organized motions, i.e.,

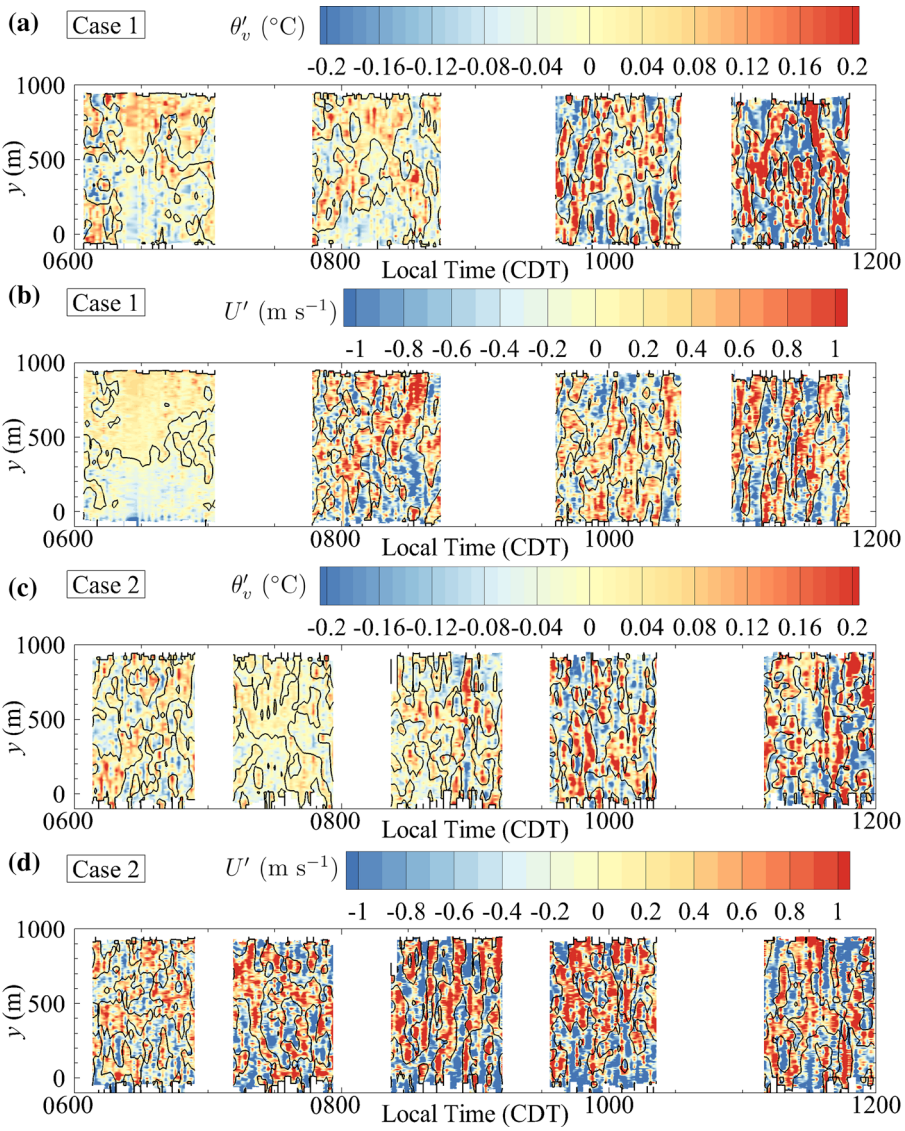

Fig. 6 Isocontours of **a** $\theta_v'(t, y)$ measured by fixed-wing UAS flying at $z = 50$ m for Case 1 with corresponding isocontours of $U'(t, y)$ shown in (**b**). Case 2 isocontours of $\theta_v'(t, y)$ and $U'(t, y)$ at $z = 50$ m shown in (**c**, **d**), respectively. The black line on the figures indicates the zero-level contour line for same data after low-pass filtering at $y \approx 200$ m in space and $t \approx 180$ s in time

coherent structures (Harun and Reda Lotfy 2019). To investigate this larger-scale organization, we treat each transect as an independent realization. We first let i be an integer value indicating transect number. We then consider two variables of interest measured in the direction of the transect, y, e.g., $\xi(y, i)$ and $\zeta(y, i)$. The cross-correlation of ξ and ζ then could be found using

$$R_{\xi\zeta}(\Delta y, \Delta i) = \left\langle \frac{\xi'(y,i)}{\langle \xi'(y,i)^2 \rangle^{1/2}} \frac{\zeta'(y+\Delta y, i+\Delta i)}{\langle \zeta'(y+\Delta y, i+\Delta i)^2 \rangle^{1/2}} \right\rangle, \tag{6}$$

where the $\langle\ \rangle$ brackets again indicate an average of values measured along the transect path. Furthermore, $R_{\xi\xi}(\Delta y, \Delta i)$ is an autocorrelation. Each transect i was correlated with neighbouring transects in the available range of Δi and ensemble-averaging applied across all i to produce an averaged correlation for the entire flight, $\langle\langle R_{\xi\zeta}(\Delta y, \Delta i)\rangle\rangle$, a process which was implemented to improve the statistical convergence of the correlations. Here, $\langle\langle\ \rangle\rangle$ indicates an average over the entire flight as opposed to an individual transect. To convert the transect separation Δi into a time displacement, Δt, we multiply by the average temporal duration of each transect for that flight.

As could be expected from Fig. 6, the most correlated motions were for scales smaller than the transect length due to turbulent motions smaller than about 500 m in spatial scale. To examine temporal and altitude trends of these motions, autocorrelations of U, $\langle\langle R_{UU}(\Delta y, 0)\rangle\rangle$, are presented in Fig. 7.

Figure 7a, b compares the time-dependence of $\langle\langle R_{UU}(\Delta y, 0)\rangle\rangle$ measured at $z = 50$ m, for Case 1 and Case 2 respectively. For Case 1 (Fig. 7a), which had higher $|Ri|$ due to reduced wind speed, there is a noticeable trend in time consisting of a broadening of the correlations in time despite the decorrelation scale (the Δy value where $\langle\langle R_{UU}\rangle\rangle \rightarrow 0$) being nearly constant for all cases where $Ri < 0$. Note that the broadening of $\langle\langle R_{UU}\rangle\rangle$ at low correlation values for the 0600 LT to 0700 LT measurement period is consistent with a weak correlation influenced by a broad background trend, as could be expected from the topographic influence observed in the visualizations of Fig. 6b. The gradual broadening of the correlations between 0700 LT and 1200 LT is also consistent with the decrease in Ri and reflects the development and growth of turbulent thermals observed in Figs. 5a, b and 6b, c. Conversely, the lower $|Ri|$ for Case 2 shows a step change in behaviour with stable and transitional Ri conditions having a similar structure with decorrelation scale of $\Delta y \approx 150$ m and unstable conditions having a similar, but slightly broader correlation with decorrelation scale of $\Delta y \approx 250$ m. The increased scales relative to Case 1 reflect the increased importance of mechanical turbulence for this case, with the more rapid transition in correlation similar to the more rapid increase in $\langle k \rangle$ shown in Fig. 3f and more rapid change in $\langle P \rangle / \langle \epsilon \rangle$ shown in Fig. 3j.

Figure 7c, d compare $\langle\langle R_{UU}(\Delta y, 0)\rangle\rangle$ measured at different altitudes between 0600 LT and 0700 LT for Case 1 and Case 2, respectively. There is a distinct difference in behaviour for the two cases, with the more stable Case 1 showing an increase in correlation with altitude similar to the behaviour reported in Alcayaga et al. (2020), with Case 2 being nearly constant with altitude. Although the increase with altitude in Case 1 could be attributed to difference in advection velocity with altitude, similar velocity gradients were present for Case 2 (Fig. 3c, d), suggesting that the difference between Fig. 7c, d reflects an altitude dependence in turbulent scales for Case 1 that is not present in Case 2. Such altitude dependence in Case 1 is consistent with a z-dependent mixing length. Such z-dependent mixing length has been reported and investigated previously in the literature (Deardorff 1980; Honnert et al. 2021). However, the reduced altitude dependence observed for Case 2 indicates the presence of large eddies which span the depth of the surface layer and potentially a boundary-layer-thickness-dependent, large-scale mixing length which coincides with what was reported by Honnert et al. (2021).

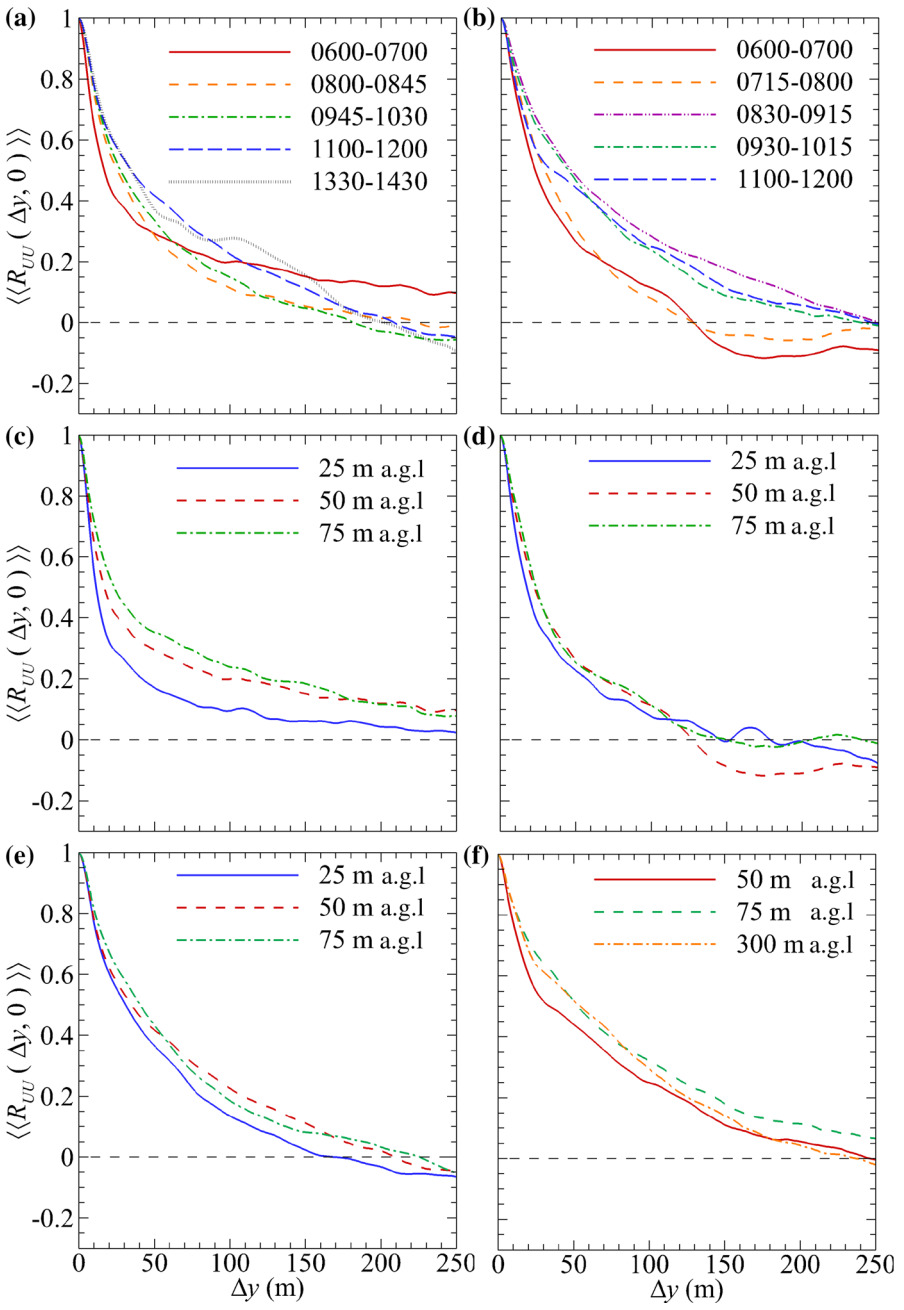

Fig. 7 Autocorrelations $\langle\langle R_{UU}(\Delta y, 0)\rangle\rangle$ measured at $z = 50$ m for **a** Case 1 and **b** Case 2 at different times. $\langle\langle R_{UU}(\Delta y, 0)\rangle\rangle$ measured between 0600 LT to 0700 LT at different altitudes for shown in (**c**) for Case 1 and and (**d**) for Case 2. $\langle\langle R_{UU}(\Delta y, 0)\rangle\rangle$ measured from 1100 LT to 1200 LT at different altitudes shown in (**e**) for Case 1 and (**f**) for Case 2

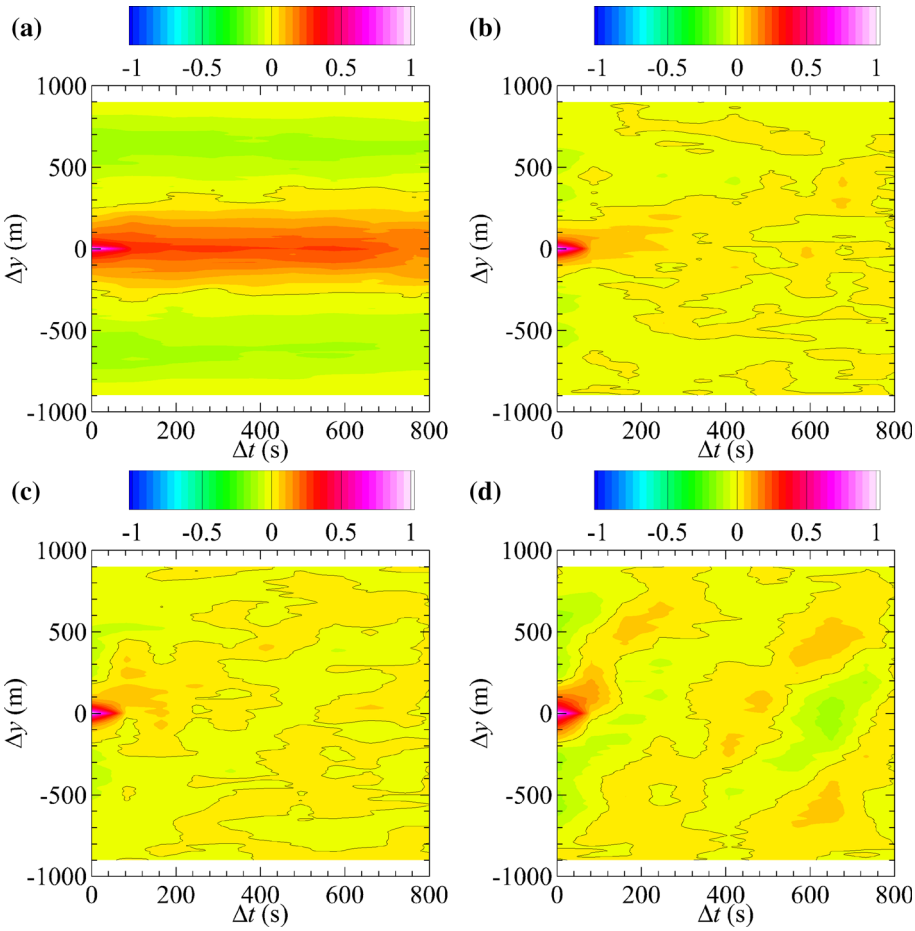

Fig. 8 Contours indicating magnitude of $\langle\langle R_{UU}(\Delta y, \Delta t)\rangle\rangle$ using observations made during Case 1 at $z = 50$ m from **a** 0600 LT to 0700 LT; **b** 0800 LT to 0845 LT; **c** 0945 LT to 10300 LT; and **d** 1100 LT to 1200 LT. Solid lines indicate where $\langle\langle R_{UU}\rangle\rangle = 0$

A similar comparison of $\langle\langle R_{UU}(\Delta y, 0)\rangle\rangle$ is made for the 1100 LT to 1200 LT time period in Fig. 7e, f. These correlations confirm that similar layer-spanning structures exist for both cases once convective conditions set in, consistent with the visualizations shown in Fig. 5. Furthermore, Case 2 shows that similar structure persists at least up to $z = 300$ m, the highest altitude measured during these observations.

To better extract the spatio–temporal organization of the velocity and temperature fields, we can examine the presence of correlated wind perturbations in contours of $\langle\langle R_{UU}(\Delta y, \Delta t)\rangle\rangle$ as provided for Case 1 in Fig. 8a–d. Note that autocorrelations such as these will be anti-symmetric in time so only the positive time displacements are shown. For the 0600 LT to 0700 LT period (Fig. 8a) there is a peak in correlation at $\Delta y = 0$ for all Δt. The persistence of these weakly correlated regions at large Δt suggest the presence of large-scale persistent structure with the Δy extent of these correlations can be considered a representative scale of the motions.

The consistent peak at $\Delta y = 0$ for the 0600 LT to 0700 LT period reflects a condition where the same flow features are being measured across each transect, which here can be

attributed to time-independent flow features produced by topographic effects (Fig. 6b). This spatially consistent structure is still present in the correlations measured from 0800 LT to 0845 LT (Fig. 8b), however now the level of correlation is much weaker, reflecting a breakup of the topographically induced motions.

Interestingly, from 0800 LT to 0845 LT (Fig. 8b) spatial periodicity becomes evident. Moreover, as the morning progresses (Fig. 8c, d) these positively correlated regions are flanked by anti-correlated regions, a feature consistent with correlations connected to VLSMs/superstructures (see for example Hutchins and Marusic 2007; Monty et al. 2007).

In the correlations from 0800 LT to 0845 LT there is some evidence of time-dependence in the correlated features, appearing as a tilt in the isocontours. This time-dependence represents a relatively slow advection in the y direction with $\Delta y/\Delta t \approx 0.5$ m s^{-1}, or about 10% of the the corresponding value of $\langle v \rangle$. The time-dependence increases as the surface layer becomes more unstable as shown in Fig. 8c, d. However, this time-dependence still suggests advection speeds of the structures are much less than the mean flow speed, approximately 20% and 50% for the 1100 LT to 1200 LT and 1330 LT to 1430 LT measurements, respectively. Similar time-dependence in the correlations was observed for the other measurement altitudes.

Similar structure and scales were observed in the temperature correlations, as illustrated in the corresponding $\langle\langle R_{\theta_v\theta_v}(\Delta y, \Delta t)\rangle\rangle$ fields shown in Fig. 9a–d. Specifically, an increase in the time-dependence of the $\langle\langle R_{\theta_v\theta_v}(\Delta y, \Delta t)\rangle\rangle$ field can be observed, which increasingly tilts relative to horizontal ($\Delta y = 0$) axis as the surface-layer transitions through neutral to convective conditions. Interestingly, for the 0800 LT to 0845 LT case (Fig. 9b) there is less evidence of long-time-scale advection although some small-scale correlated features appear which have $\Delta y/\Delta t$ on the order of 50% of the mean velocity.

There are some interesting implications of this observation of varying advection velocity with time and surface-layer stability. It should be noted that, due to the measurements being conducted as a transect rather than over a spatial plane, we cannot rule out that these measurements reflect the presence of long advected structures, which are being bisected by the aircraft. In such a case, the time-dependence of the advection velocity could represent a change in the angle of the structure with respect to the transect direction (assuming it advects with the mean velocity), rather than a change in advection velocity. Alternatively, this change in advection velocity could reflect changes in the physical process of structure formation, with the more stable conditions producing structures that are evolving more slowly and dependent on surface features which produce them. Regardless, the result confirms that for this type of flow the application of Taylor's frozen-flow hypothesis to reconstruct the spatial structure of large-scale flow features could confound interpretation, as reviewed by Moin (2009) and many others for canonical wall-bounded flow.

To confirm that these coherent motions play an important role in the turbulent transport of momentum and heat (as previously reported in for example Gao et al. 1989; Lu and Fitzjarrald 1994; Drobinski et al. 2004; Feigenwinter and Vogt 2005; Barthlott et al. 2007) we look at the the cross-correlation fields of $\langle\langle R_{u^*w}(\Delta y, \Delta t)\rangle\rangle$ and $\langle\langle R_{w\theta_v}(\Delta y, \Delta t)\rangle\rangle$. Here, to all we've introduced a mean-flow aligned coordinate system (x^*, y^*, z) and (u^*, v^*, w) whereby the coordinate system has been rotated to align x^* with the mean wind vector. Examples of these cross-correlation fields are shown in Fig. 10 and reveal the same general structure as observed in the $\langle\langle R_{UU}(\Delta y, \Delta t)\rangle\rangle$ and $\langle\langle R_{\theta_v\theta_v}(\Delta y, \Delta t)\rangle\rangle$ autocorrelation fields. Specifically, the time-dependence of the isocontours, reflecting the same $\Delta y/\Delta t$ dependence observed in the velocity and temperature autocorrelations.

These structures also show the expected turbulent transport behaviour of negative momentum flux (reflected in negative $\langle\langle R_{u^*w}\rangle\rangle$ at $(\Delta y, \Delta t) = (0, 0)$) for Fig. 10a, c and positive buoyancy flux (reflected in positive $\langle\langle R_{w\theta_v}\rangle\rangle$ at $(\Delta y, \Delta t) = (0, 0)$) for Fig. 10b, d. Notably

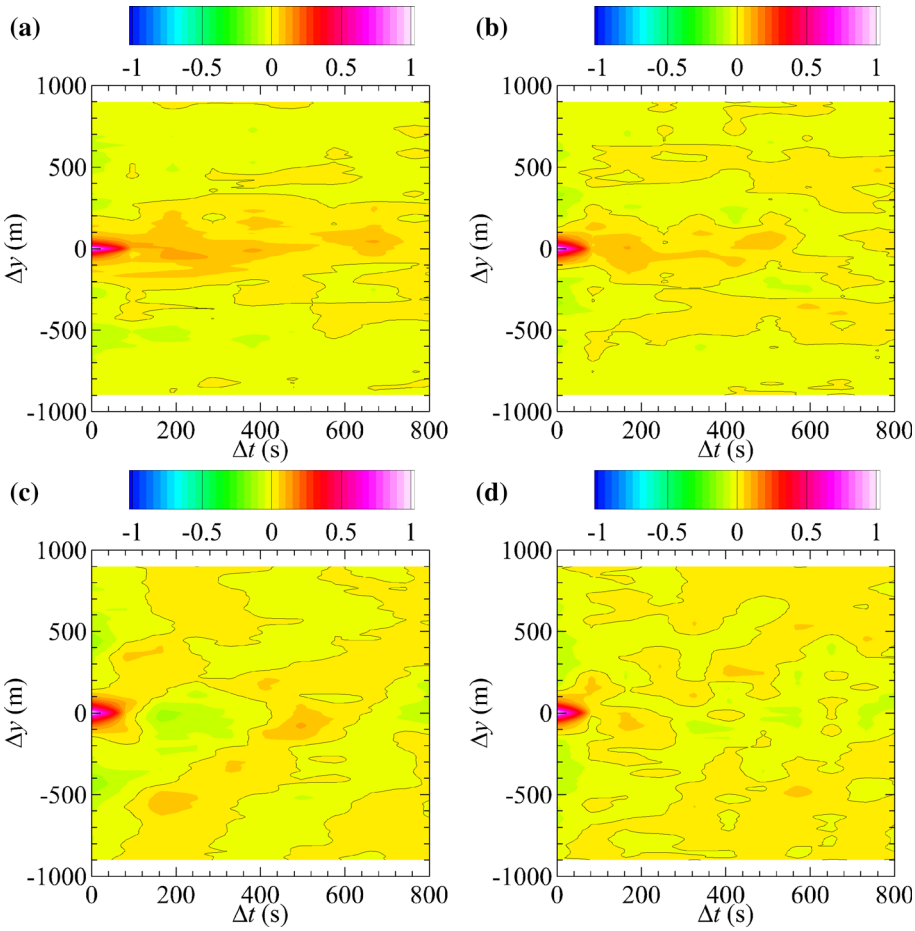

Fig. 9 Contours indicating magnitude of $\langle\langle R_{\theta_v\theta_v}(\Delta y, \Delta t)\rangle\rangle$ using observations made during Case 1 at $z =$ 50 m from **a** 0600 LT to 0700 LT; **b** 0800 LT to 0845 LT; **c** 0945 LT to 1030 LT; and **d** 1100 LT to 1200 LT. Solid lines indicate where $\langle\langle R_{\theta_v\theta_v}\rangle\rangle$=0

these regions of negative $\langle\langle R_{u^*w}\rangle\rangle$ and positive $\langle\langle R_{w\theta_v}\rangle\rangle$ are consistent with same length and width scales observed in the autocorrelations.

Finally, we note that similar behaviour was observed for the results from Case 2 (not presented for the sake of brevity). However, the organization of the weakly correlated motions was a little less clear. This reduced clarity is likely due to the increased small-scale activity during Case 2, which required more measurement time than available to achieve sufficient statistical convergence to resolve the underlying coherent motions. One distinct difference noted between Case 1 and Case 2 was that during the 0600 LT to 0700 LT flight for Case 2 the correlations showed evidence of the same large-scale structure observed during the neutral and convective conditions of Case 1.

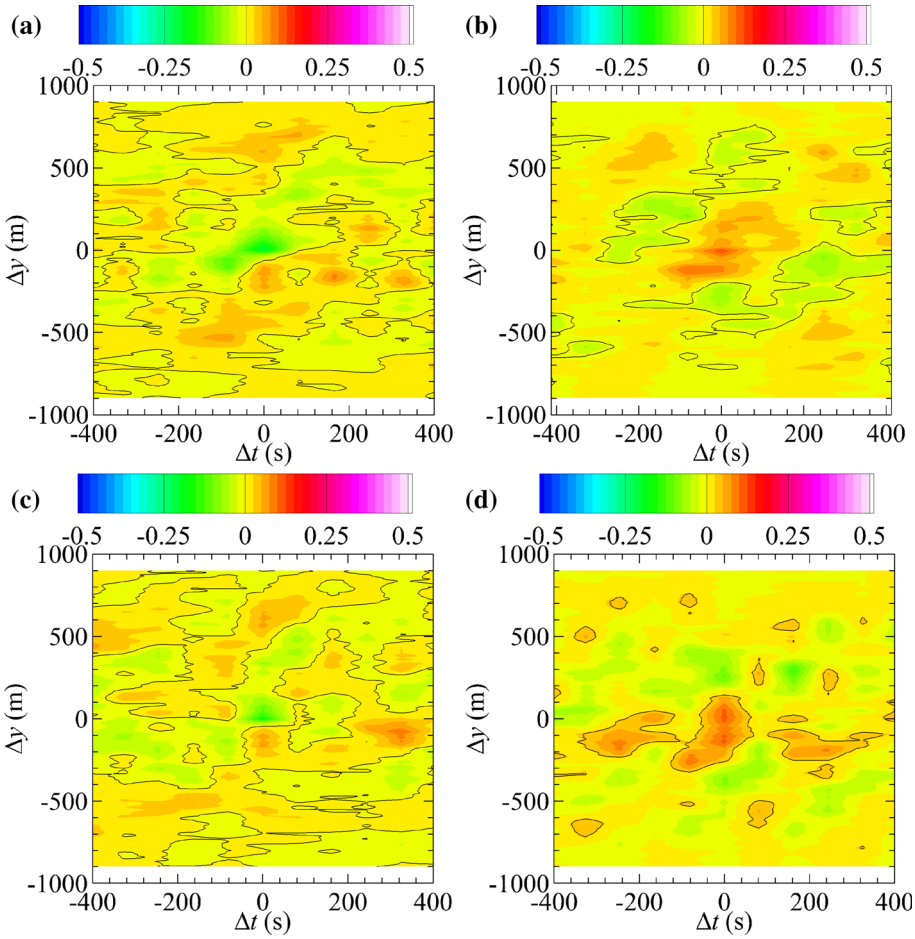

Fig. 10 Contours indicating magnitude of **a** $\langle\langle R_{u^*w}(\Delta y, \Delta t)\rangle\rangle$ and **b** $\langle\langle R_{w\theta_v}(\Delta y, \Delta t)\rangle\rangle$ measured between 0945 LT and 1030 LT using observations made at $z = 50$ m during Case 1. $\langle\langle R_{u^*w}(\Delta y, \Delta t)\rangle\rangle$ and $\langle\langle R_{w\theta_v}(\Delta y, \Delta t)$ measured between 1100 LT and 1200 LT shown in (**c**, **d**), respectively

3.5 Coherent Structure Associated with Sweep and Ejection Events

The previous section demonstrated statistical signatures in correlation fields consistent with the existence of coherent structures at spatial scales on the order of 100 m and temporal scales exceeding 10 min. This included correlation between the vertical and horizontal velocity, which is classically organized into ejection and sweep events (see, for example Robinson 1991) corresponding to negative $\overline{u^{*\prime}w^{\prime}}$ events having positive $w^{\prime}$ (ejections) and negative $w^{\prime}$ (sweeps). Here we utilize the unique nature of the UAS data to examine the structure of these events in greater detail. Specifically, we note that the use of UAS provides an opportunity to better understand the spatial scale of these structures in the atmospheric surface layer due to their ability to minimize the impact of advection velocity on the measurement of flow structure.

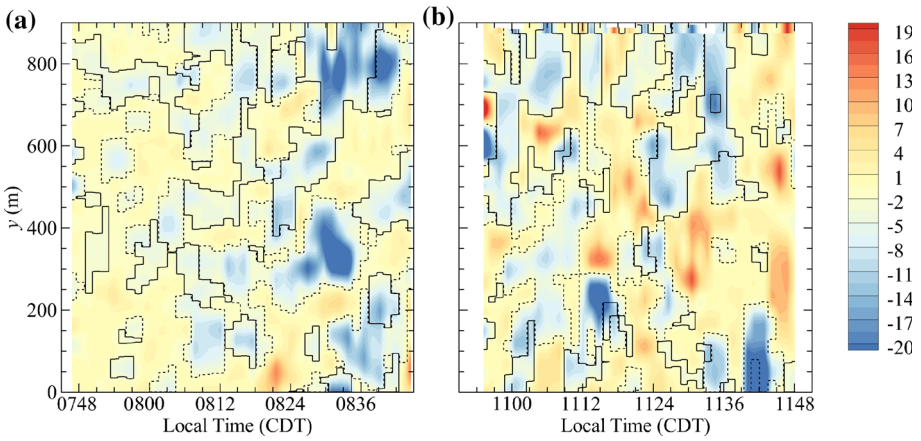

Fig. 11 Contours of low-pass filtered $u^{*\prime}w'/u_\tau^2$ from observations made at $z = 50$ m **a** measured between 0800 LT and 0845 LT during Case 1 and **b** measured between 1100 LT and 1200 LT during Case 1. Solid lines indicate identified sweep events, dashed lines indicate identified ejection events

We first look at the spatio–temporal distribution of $u^{*\prime}w'/u_\tau^2$. Examples are shown in Fig. 11 from Case 1, specifically the distributions measured between 0800 LT and 0845 LT and between 1100 LT and 1200 LT. Note that, to better isolate the large-scale coherent motions, the $u^{*\prime}(t)$ and $w'(t)$ fields were first low-pass filtered at 1 Hz (filtering out motions smaller than approximately 20 m). The results shown in Fig. 11a reflect the prominence of the negative $u^{*\prime}w'$ events relative to the positive events in the more mechanically driven, near-neutral stability conditions. Later in the morning (Fig. 11b), more large-scale positive $u^{*\prime}w'$ events were observed, but there is still a preponderance of negative $u^{*\prime}w'$ events measured over the same time period.

A procedure was developed to identify sweep and ejection events from these spatio-temporal fields. First, to identify individual ejection events, the low-pass-filtered spatio-temporal regions having magnitude of $u^{*\prime}w' < -0.05$ and $w' > 0$ were identified. Note that the results were found to be largely insensitive to the threshold selected and -0.05 was selected as it proved a large enough value to reject events too short in duration to be considered 'coherent' while also being small enough in magnitude to not filter out larger-scale events. Finally, individual ejection events were isolated by identifying groups of connected measurement points meeting this criterion. To identify individual sweep events, the same procedure was applied, but constrained to $w' < 0$ events.

The results of this identification process are shown in Fig. 11 using solid lines to indicate identified sweep events and dashed lines to indicate identified ejection events. The results show a roughly equal distribution of sweep and ejection events. In addition, it appears that several of the larger events are composed of numerous smaller-scale events, which could signal the formation of a larger-scale structure through alignment of smaller structures, similar to the mechanisms proposed for the formation of very-large-scale motions or superstructures in canonical wall-bounded flow (Monty et al. 2007; Hutchins and Marusic 2007). Alternatively, recognizing Fig. 11 represents a spatio–temporal field, these multiple instances could be the same event bisected by the aircraft at different times and may represent temporal evolution of the structure as it advects through the measurement region.

To highlight the importance of these structures to the overall turbulence intensity and transport, we evaluated the contributions of the regions encapsulated by these events to the

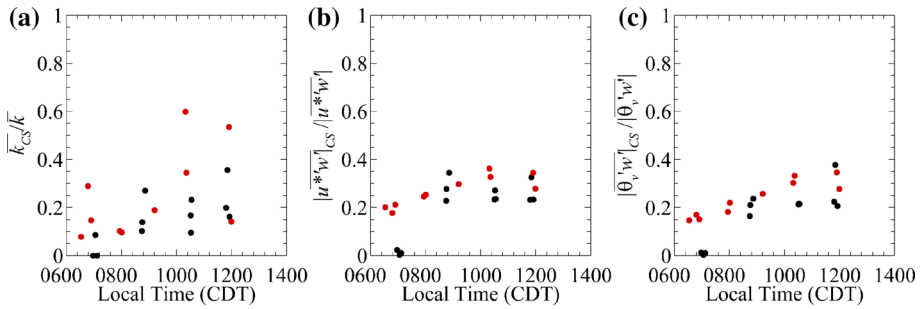

Fig. 12 Contribution towards total **a** turbulence kinetic energy; **b** momentum flux; and **c** sensible heat flux by ejection and sweep events. Black dots indicate Case 1 and red dots indicate Case 2

k, $\langle u^{*\prime} w^{\prime} \rangle$, and $\langle \theta_v^{\prime} w^{\prime} \rangle$ measured over the entire flight. This was done by setting the portions of the filtered $u^{\prime}$, $v^{\prime}$, $w^{\prime}$ and $\theta_v^{\prime}$ time series that fell outside the identified sweep/ejection regions to zero, and calculating $\overline{k}_{CS}$, $\overline{|u^{*} w|}_{CS}$ and $\overline{|\theta_v w|}_{CS}$ from the time series measured during the flight. Here, the subscripted CS is used to indicate values determined using only measurements from within an identified sweep or ejection event. These values were then compared to the corresponding values of $\overline{k}$, $\overline{|u^{*} w|}$ and $\overline{|\theta_v w|}$ determined from the unfiltered data and without nullifying the portions of the time series falling outside the sweeps and ejections.

The resulting ratios of $\overline{k}_{CS}/\overline{k}$, $\overline{|u^{*} w^{\prime}|}_{CS}/\overline{|u^{*} w|}$ and $\overline{|\theta_v^{\prime} w^{\prime}|}_{CS}/\overline{|\theta_v^{\prime} w^{\prime}|}$ are presented in Fig. 12a–c, respectively. In general, the results show that the contribution from the coherent motions increases over the course of the morning, with good agreement between the cases. Although there is significant scatter in the $\overline{k}_{CS}/\overline{k}$ results, this estimate suggests that the sweep and ejection motions account for as much as 10% to 20% of the turbulence kinetic energy and 20% to 30% of the momentum and sensible heat flux. This is comparable to what has previously been reported by Feigenwinter and Vogt (2005) and Barthlott et al. (2007), but much lower than reported by Gao et al. (1989), for example.

The contribution of individual coherent structures to the momentum flux was expanded upon by examining the minimum value of $u^{*\prime} w^{\prime}$ measured within each individual sweep and ejection event. Furthermore, we also compare these minimum values to the y-direction (nominally streamwise) scale of each corresponding sweep and ejection event, δy. The results of this comparison are shown in Fig. 13a, b for sweep and ejection events respectively. Despite significant scatter, several observations can be made from these figures. The first is that there is a clear correlation between the scale of the structure and the magnitude of $(u^{*\prime} w^{\prime})/u_{\tau}^2$ produced within it. A second observation is that sweeps and ejections have similar scales, although there is more variability in the size of the ejection events. There does seem to be qualitative evidence in Fig. 13a, b that, given the smaller u_{τ} occurring earlier in the transition process, the reduced convective activity allows larger structures to form but with a corresponding weaker momentum flux. As the buoyant forcing increases the structures become smaller in scale, but with a corresponding increase in momentum flux.

Finally, to examine the changes in structure of the sweep and ejection events over the course of the morning transition, conditional averaging was conducted. This procedure utilized the same sweep/ejection identification procedure described above but, to minimize the influence of alignment of multiple structures influencing the averaging process, a more restrictive $u^{*\prime} w^{\prime}$ threshold of 80% the minimum measured during each transect was employed. For each individual structure, it's spatial, δy, and temporal, δt, extents were determined. Each

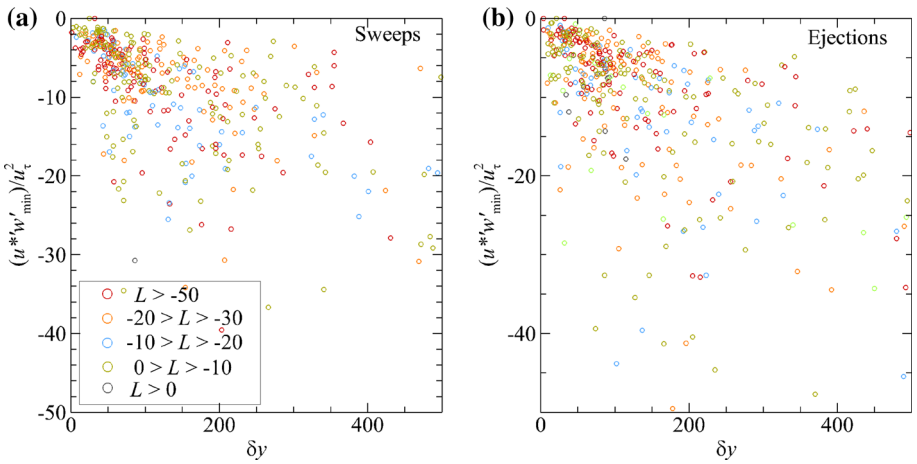

Fig. 13 Comparison of approximate scale of observed sweep and ejection events to estimated magnitude of momentum flux contribution

structure was then re-scaled by $y/\delta y$, $t/\delta t$ and $(u', v', w')/(|u^{*\prime}w'_{min}|)^{0.5}$ before averaging all identified structures. Here, $|u^{*\prime}w'_{min|}$ is the minimum value of the shear stress within each structure. The result being an average structure scaled by its peak momentum flux and spatial and temporal extents.

Conditionally averaged velocity vectors corresponding to ejection events are shown in Fig. 14 from Case 1, with the events measured from 0800 LT to 0845 LT shown in (*a*) and from 1100 LT to 1200 LT shown in (*b*). Although not many events were averaged, some interesting observations can be made. Focusing first on the averaged structure from the earlier morning measurements (Fig. 14a), we see evidence of the ejection event flanked by counter-rotating vortex structure at $z = 75$ m. To better illustrate this we also present the corresponding isocontours of the pseudo-vorticity

$$\tilde{\omega} = \left(\frac{\partial v}{\partial t}\delta t - \frac{\partial u}{\partial y}\delta y\right)\frac{1}{(|u^{*\prime}w'|_{min|})^{0.5}} \tag{7}$$

in Fig. 14c. Although only an approximate estimate of the z-aligned component of vorticity, these results do suggest the presence of a counter rotational structure extended throughout the measurement plane. This counter-rotating structure is consistent with the observations from zero-pressure-gradient isothermal boundary layers (e.g., Adrian 2007) of ejection events corresponding to hairpin vortex formation and streamwise vorticity near the surface. Further corroborating the similarity of this structure with the canonical turbulent boundary layer structure is that these ejection events appear to be preceded by upstream sweep events events at higher elevations as described by Robinson (1991).

The conditionally-averaged structures from the later morning/convective boundary layer conditions (Fig. 14b) are less well-defined. However, some similarities between this structure and that of the earlier morning are evident. Most notably, in the appearance of precedent sweeping events at $z = 75$ m and the indication of counter-rotating vorticity in the corresponding pseudo-vorticity contours of Fig. 14d.

For the sweep events, conditionally averaged velocity vectors corresponding are shown in Fig. 15a, b from Case 1, with the events measured from 0800 LT to 0845 LT shown in (*a*) and from 1100 LT to 1200 LT shown in (*b*). The corresponding $\tilde{\omega}$ corresponding to the results are

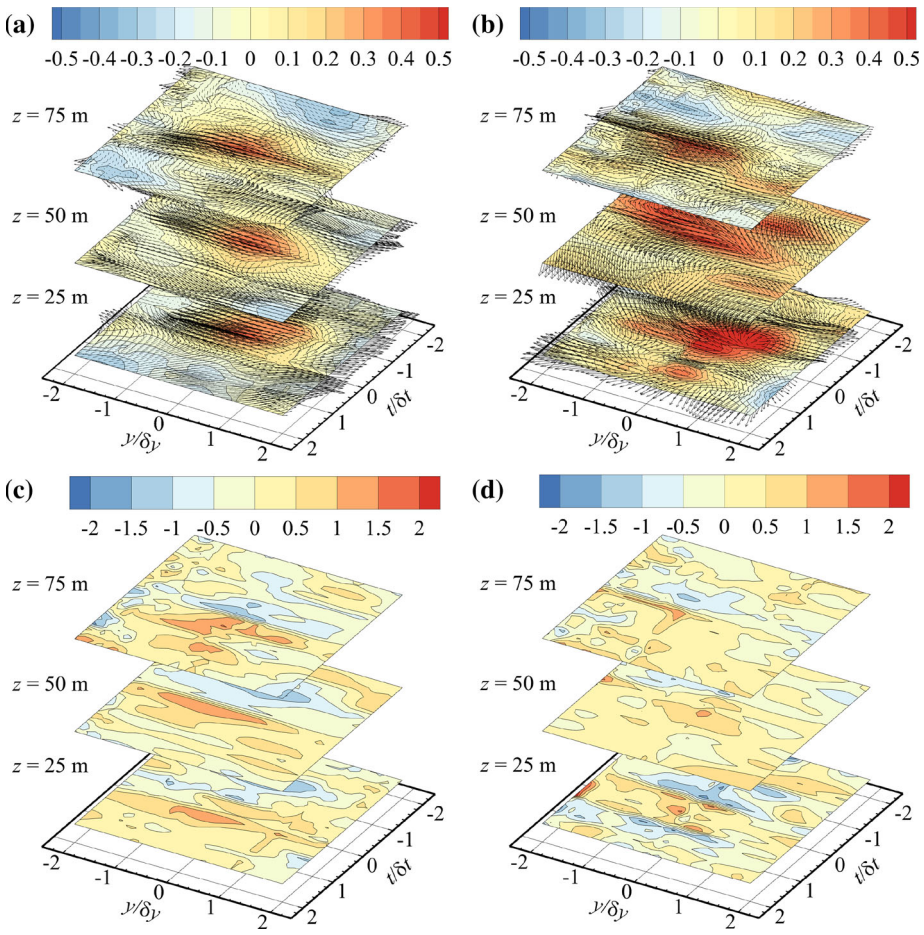

Fig. 14 Conditionally averaged velocity vectors of ejection events from observations **a** measured between 0800 LT and 0845 LT during Case 1 and **b** measured between 1100 LT and 1200 LT during Case 1. Contours in (**a**, **b**) are of $w'/(|u^{*\prime}w'|_{min}|)^{0.5}$. Contours of $\tilde{\omega}$ corresponding to the results shown in (**a**, **b**) are shown in (**c**, **d**) respectively

shown in Fig. 15c, d. In general, conditionally-averaged sweep structures display much less organization than the corresponding ejection structure. One notable pattern, however, is that as the surface is approached, the portion of δt and δy encompassed by the negative vertical velocity appears to increase, even though a comparison δt, δy and $(|u^{*\prime}w'|_{min})^{0.5}$ across the three heights indicates that these scaling factors are approximately the same. This then suggests a spreading of the event as it approaches the surface, reminiscent of a 'splatting' event. Evidence of counter rotation structure flanking the sweep events is also present in the contours of $\tilde{\omega}$, most notably in the 0800 LT to 0845 LT results shown in Fig. 15c.

4 Discussion and Conclusions

Stationary (in situ) measuring devices are commonly used to infer turbulence structure. However, this usually necessitates inferring the wind's spatial distribution using Taylor's

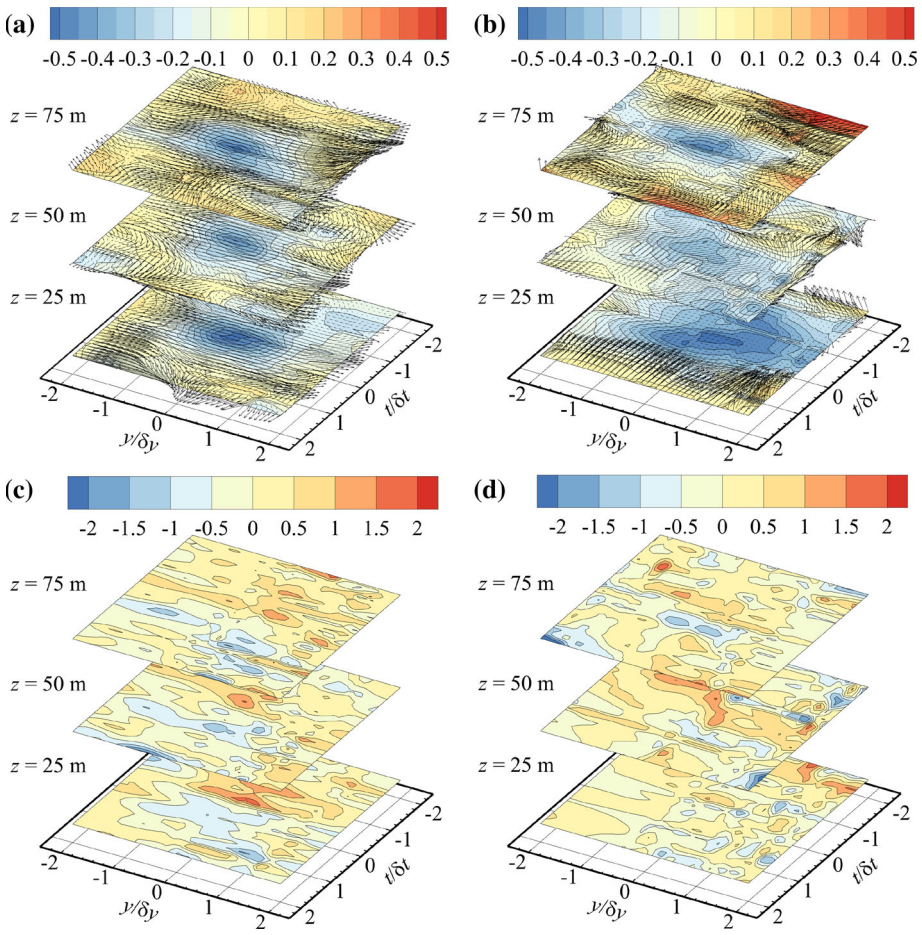

Fig. 15 Conditionally averaged velocity vectors of sweep events from observations **a** measured between 0800 LT and 0845 LT during Case 1 and **b** measured between 1100 LT and 1200 LT during Case 1. Contours in (**a**, **b**) are of $w'/(|u^{*\prime}w'|_{min}|)^{0.5}$. Contours of $\tilde{\omega}$ corresponding to the results shown in (**a**, **b**) are shown in (**c**, **d**) respectively

frozen-flow theory, which is poorly realized at large scales, particularly in non-stationary flows subject to the diurnal stability cycle. Multiple synchronous measuring systems at different sites are used to solve this limitation. On the other hand, UASs are becoming more common in atmospheric research. These can travel through the flow on time scales quicker than coherent structures, resulting in improved spatial resolution of the turbulence structure along the flight path. Furthermore, because of their lower cruising speed compared to crewed aircraft, UASs can obtain measurements with high spatial resolution while simultaneously sampling temporally. This study employed several UASs to investigate the structure of the surface layer during the morning transition acquired as a part of the 2017 CLOUDMAP measurement campaign near Stillwater, Oklahoma, USA.

Analysis of single- and multi-point statistics conducted using fixed-wing and rotorcraft UASs flying simultaneously at different altitudes and flight paths demonstrated the potential for UAS to resolve coherent structures within the atmospheric surface layer. Generally, similar evolution was observed in the single-point statistics over the two cases measured, although decreased stability was present during Case 2, which resulted in significantly more influence of mechanical production for that case. The increased mechanical production corresponded to a reduction in temperature gradients and increased turbulence kinetic energy. Visualizations of the velocity and temperature fields connected these changes to a clear increase in the variability in both the vertical and horizontal fields. These visualizations also reflected the formation of turbulent thermals on the scale of hundreds of metres which became stronger as the morning evolved. Visualizations of the horizontal plane also appeared to indicate the presence of larger-scale motion. Application of spatio–temporal correlations to quasi-streamwise transects through the surface layer indicated that the structures have streamwise extent of approximately 200-m long, which grew with distance from the surface but reduced in streamwise scale over the course of the morning. Importantly, these spatio–temporal correlations provided a mean to measure the average advection velocity of the coherent structures. The results indicated the advection velocity was significantly lower than the mean velocity and only 20% to 50% of the mean velocity. This ratio was time dependent and increased with the increase in convective activity. One explanation for the presence of such low advection velocity is that the shear driven structures may form locally (i.e., are 'attached' to the surface) potentially formed by local topography. This process is decoupled from the surface as the buoyant forcing increases.

By taking kinetic energy from the mean flow and transferring it to smaller scales in the form of more isotropic movements, coherent structures can operate as an intermediary in the inertial cascade process. Here, by isolating ejection and sweep events, we found that these structures contribute approximately 20% to 30% of overall turbulence kinetic energy, momentum, and sensible heat flux, with an increase observed during the course of the boundary-layer transition. This result is at the lower end of published estimates which have a broad range of suggested values ranging between 30% to 70%. It should be noted that these UAS measurements are only capable of resolving motions smaller than the transect length (approximately 1 km) and time-dependent fluctuations in the measured turbulence kinetic energy from each transect suggests that larger-scale motions (with time scales on the order of 30 min) were present. Thus, this low estimate of contributions could be due to the comparatively short transect length preventing filtering out the contribution of scales of motion larger than half the transect length.

Finally, the spatio–temporal organization of the coherent motions was educed by employing a conditional-averaging process. Although the limited number of events captured resulted in weak statistical convergence, there was evidence of similarities between the structure of ejection events observed in the atmospheric surface layer, and structures observed in canonical zero-pressure-gradient isothermal turbulent boundary layers. This organization weakened with increased buoyant forcing, but similarities did persist. Less organization was observed in the sweeping events, although there was evidence of splatting as the event reached the surface.

Acknowledgements This work was supported by the US National Science Foundation through Awards No. CBET-1351411, 1539070, and CNS-1932105.

Data Availability The datasets generated during and/or analysed during the current study are available from the corresponding author on reasonable request.

Declarations

Conflict of interest The authors have no competing interests to declare that are relevant to the content of this article.

References

Adrian RC, Meinhart CD, Tomkins CD (2000) Vortex organization in the outer region of the turbulent boundary layer. J Fluid Mech 422:1–54

Adrian RJ (2007) Hairpin vortex organization in wall turbulence. Phys Fluids 19(4):041301. https://doi.org/10.1063/1.2717527

Al-Ghussain L, Bailey SCC (2021) An approach to minimize aircraft motion bias in multi-hole probe wind measurements made by small unmanned aerial systems. Atmos Meas Tech 14(1):173–184. https://doi.org/10.5194/amt-14-173-2021

Alcayaga L, Larsen GC, Kelly M, Mann J (2020) Large-scale coherent structures in the atmosphere over a flat terrain. J Phys Conf Ser. https://doi.org/10.1088/1742-6596/1618/6/062030

Bailey SCC, Canter CA, Sama MP, Houston AL, Smith SW (2019) Unmanned aerial vehicles reveal the impact of a total solar eclipse on the atmospheric surface layer. Proc R Soc A Math Phys Eng Sci. https://doi.org/10.1098/rspa.2019.0212

Balakumar BJ, Adrian RJ (2007) Large- and very-large-scale motions in channel and boundary-layer flows. Philos Trans R Soc A 365:665–681

Balsley BB, Lawrence DA, Woodman RF, Fritts DC (2013) Fine-scale characteristics of temperature, wind, and turbulence in the lower atmosphere (0–1,300 m) over the South Peruvian Coast. Boundary-Layer Meteorol 147(1):165–178. https://doi.org/10.1007/s10546-012-9774-x

Bange J, Spieß T, van den Kroonenberg A (2007) Characteristics of the early-morning shallow convective boundary layer from Helipod Flights during STINHO-2. Theor Appl Climatol 90(1–2):113–126. https://doi.org/10.1007/s00704-006-0272-2

Barbieri L, Kral ST, Bailey SCC, Frazier AE, Jacob JD, Reuder J, Brus D, Chilson PB, Crick C, Detweiler C, Doddi A, Elston J, Foroutan H, González-Rocha J, Greene BR, Guzman MI, Houston AL, Islam A, Kemppinen O, Lawrence D, Pillar-Little EA, Ross SD, Sama MP, Schmale DG, Schuyler TJ, Shankar A, Smith SW, Waugh S, Dixon C, Borenstein S, Boer GD (2019) Intercomparison of small unmanned aircraft system (sUAS) measurements for atmospheric science during the LAPSE-RATE campaign. Sensors (Switzerland). https://doi.org/10.3390/s19092179

Bärfuss K, Pätzold F, Altstädter B, Kathe E, Nowak S, Bretschneider L, Bestmann U, Lampert A (2018) New setup of the UAS ALADINA for measuring boundary layer properties. Atmos Part Solar Radiat Atmos 9(1):28. https://doi.org/10.3390/atmos9010028

Barthlott C, Drobinski P, Fesquet C, Dubos T, Pietras C (2007) Long-term study of coherent structures in the atmospheric surface layer. Boundary-Layer Meteorol 125(1):1–24. https://doi.org/10.1007/s10546-007-9190-9

Bennett LJ, Weckwerth TM, Blyth AM, Geerts B, Miao Q, Richardson YP (2010) Observations of the evolution of the nocturnal and convective boundary layers and the structure of open-celled convection on 14 June 2002. Mon Weather Rev 138(7):2589–2607. https://doi.org/10.1175/2010MWR3200.1

Blackwelder R, Kaplan R (1976) On the wall structure of the turbulent boundary layer. J Fluid Mech 76:89–112

Boppe RS, Neu WL, Shuai H (1999) Large-scale motions in the marine atmospheric surface layer. Boundary-Layer Meteorol 92:165–183

Brown GL, Roshko A (1974) On density effects and large structure in turbulent mixing layers. J Fluid Mech 64(4):775–816. https://doi.org/10.1017/S002211207400190X

Chauhan K, Hutchins N, Monty J, Marusic I (2013) Structure inclination angles in the convective atmospheric surface layer. Boundary-Layer Meteorol 147(1):41–50. https://doi.org/10.1007/s10546-012-9777-7

Chow F, Schär C, Ban N, Lundquist K, Schlemmer L, Shi X (2019) Crossing multiple gray zones in the transition from mesoscale to microscale simulation over complex terrain. Atmosphere 10(5):274. https://doi.org/10.3390/atmos10050274

Deardorff JW (1980) Stratocumulus-capped mixed layers derived from a three-dimensional model. Boundary-Layer Meteorol 18(4):495–527. https://doi.org/10.1007/BF00119502

Dias Júnior C, Sá L, Pachêco V, de Souza C (2013) Coherent structures detected in the unstable atmospheric surface layer above the Amazon forest. J Wind Eng Ind Aerodyn 115:1–8. https://doi.org/10.1016/j.jweia.2012.12.019

Drobinski P, Ra Brown, Flamant PH, Pelon J (1998) Evidence of organized large Eddies by ground-based Doppler Lidar. Sonic Anemom Sodar Boundary-Layer Meteorol 88(3):343–361. https://doi.org/10.1023/A:1001167212584

Drobinski P, Carlotti P, Newsom RK, Banta RM, Foster RC, Redelsperger JL (2004) The structure of the near-neutral atmospheric surface layer. J Atmos Sci 61(6):699–714

Eder F, Serafimovich A, Foken T (2013) Coherent structures at a forest edge: properties, coupling and impact of secondary circulations. Boundary-Layer Meteorol 148(2):285–308. https://doi.org/10.1007/s10546-013-9815-0

Egger J, Bajrachaya S, Heinrich R, Kolb P, Lämmlein S, Mech M, Reuder J, Schäper W, Shakya P, Schween J, Wendt H (2002) Diurnal winds in the Himalayan Kali Gandaki Valley. Part III: remotely piloted aircraft soundings. Mon Weather Rev 130(8):2042–2058. https://doi.org/10.1175/1520-0493(2002)130<2042:DWITHK>2.0.CO;2

Etling D, Brown RA (1993) Roll vortices in the planetary boundary layer: a review. Boundary-Layer Meteorol 65(3):215–248. https://doi.org/10.1007/BF00705527

Feigenwinter C, Vogt R (2005) Detection and analysis of coherent structures in urban turbulence. Theor Appl Climatol 81:219–230

Froidevaux M, Higgins CW, Simeonov V, Ristori P, Pardyjak E, Serikov I, Calhoun R, van den Bergh H, Parlange M (2012) A Raman lidar to measure water vapor in the atmospheric boundary layer. Adv Water Resour. https://doi.org/10.1016/j.advwatres.2012.04.008

Ganapathisubramani B, Longmire EK, Marusic I (2003) Characteristics of vortex packets in turbulent boundary layers. J Fluid Mech 478:35–46

Gao W, Shaw RH, Paw UKT (1989) Observation of organized structure in turbulent flow within and above a forest canopy. Boundary-Layer Meteorol 47(1–4):349–377. https://doi.org/10.1007/BF00122339

Garratt JR (1994) Review: the atmospheric boundary layer. Earth-Sci Rev 37(1–2):89–134. https://doi.org/10.1016/0012-8252(94)90026-4

González-Rocha J, De Wekker SFJ, Ross SD, Woolsey CA (2020) Wind profiling in the lower atmosphere from wind-induced perturbations to multirotor UAS. Sensors 20(5):1341. https://doi.org/10.3390/s20051341

Grachev AA, Andreas EL, Fairall CW, Guest PS, Persson POG (2013) The critical Richardson number and limits of applicability of local similarity theory in the stable boundary layer. Boundary-Layer Meteorol 147(1):51–82. https://doi.org/10.1007/s10546-012-9771-0

Gu HH, Wang GH, Zhu W, Zheng XJ (2019) Gusty wind disturbances and large-scale turbulent structures in the neutral atmospheric surface layer. Sci China Phys Mech Astron 62(11):1–7. https://doi.org/10.1007/s11433-019-9398-5

Guala M, Hommema SE, Adrian RJ (2006) Large-scale and very-large-scale motions in turbulent pipe flow. J Fluid Mech 554:521–542

Harun Z, Reda Lotfy E (2019) Generation, evolution, and characterization of turbulence coherent structures. In: Turbulence and related phenomena, vol 395, IntechOpen, pp 116–124. https://doi.org/10.5772/intechopen.76854

Head MR, Bandyopadhyay P (1981) New aspects of turbulent boundary-layer structure. J Fluid Mech 107:297–337

Hernandez-Deckers D, Sherwood SC (2016) A numerical investigation of cumulus thermals. J Atmos Sci 73(10):4117–4136. https://doi.org/10.1175/JAS-D-15-0385.1

Higgins CW, Wing MG, Kelley J, Sayde C, Burnett J, Holmes HA (2018) A high resolution measurement of the morning ABL transition using distributed temperature sensing and an unmanned aircraft system. Environ Fluid Mech 18(3):683–693. https://doi.org/10.1007/s10652-017-9569-1

Hobbs S, Dyer D, Courault D, Olioso A, Lagouarde JP, Kerr Y, Mcaneney J, Bonnefond J (2002) Surface layer profiles of air temperature and humidity measured from unmanned aircraft. Agronomie 22(6):635–640. https://doi.org/10.1051/agro:2002050

Honnert R, Masson V, Lac C, Nagel T (2021) A theoretical analysis of mixing length for atmospheric models from micro to large scales. Front Earth Sci 8(January):1–15. https://doi.org/10.3389/feart.2020.582056

Horiguchi M, Hayashi T, Adachi A, Onogi S (2012) Large-scale turbulence structures and their contributions to the momentum flux and turbulence in the near-neutral atmospheric boundary layer observed from a 213-m tall meteorological tower. Boundary-Layer Meteorol 144(2):179–198. https://doi.org/10.1007/s10546-012-9718-5

Huang J, Cassiani M, Albertson JD (2009) Analysis of coherent structures within the atmospheric boundary layer. Boundary-Layer Meteorol 131(2):147–171. https://doi.org/10.1007/s10546-009-9357-7

Hutchins N, Marusic I (2007) Evidence of very long meandering features in the logarithmic region of turbulent boundary layers. J Fluid Mech 579:1–28. https://doi.org/10.1017/S0022112006003946

Hutchins N, Hambleton WT, Marusic I (2005) Inclined cross-stream stereo particle image velocimetry measurements in turbulent boundary layers. J Fluid Mech 541:21–54

Inagaki A, Castillo MCL, Yamashita Y, Kanda M, Takimoto H (2012) Large-Eddy simulation of coherent flow structures within a cubical canopy. Boundary-Layer Meteorol 142(2):207–222. https://doi.org/10.1007/s10546-011-9671-8

Ingenhorst C, Jacobs G, Stößel L, Schelenz R, Juretzki B (2021) Method for airborne measurement of the spatial wind speed distribution above complex terrain. Wind Energy Sci 6(2):427–440. https://doi.org/10.5194/wes-6-427-2021

Iwai H, Ishii S, Tsunematsu N, Mizutani K, Murayama Y, Itabe T, Yamada I, Matayoshi N, Matsushima D, Weiming S, Yamazaki T, Iwasaki T (2008) Dual-Doppler lidar observation of horizontal convective rolls and near-surface streaks. Geophys Res Lett 35(14):L14. https://doi.org/10.1029/2008GL034571

Jacob JD, Chilson PB, Houston AL, Smith SW (2018) Considerations for atmospheric measurements with small unmanned aircraft systems. Atmosphere 9(7):1–16. https://doi.org/10.3390/atmos9070252

Jiménez J (2011) Cascades in wall bounded turbulence. Annu Rev Fluid Mech 44:27–45

Kelly RD (1982) A single Doppler radar study of horizontal-roll convection in a lake-effect snow storm. J Atmos Sci 39(7):1521–1531. https://doi.org/10.1175/1520-0469(1982)039<1521:ASDRSO>2.0.CO;2

Kim KC, Adrian RJ (1999) Very large-scale motion in the outer layer. Phys Fluids 11(2):417–422

Kim SW, Park SU (2003) Coherent structures near the surface in a strongly sheared convective boundary layer generated by large-Eddy simulation. Boundary-Layer Meteorol 106(1):35–60. https://doi.org/10.1023/A:1020811015189

Kline SJ, Reynolds WC, Schraub FA, Runstadler PW (1967) The structure of turbulent boundary layers. J Fluid Mech 30(4):741–773. https://doi.org/10.1017/S0022112067001740

Krunsche N, de Oliveira A (2004) Characterization of coherent structures in the atmospheric surface layer. Boundary-Layer Meteorol 110:191–211

Leelőssy Á, Molnár F, Izsák F, Havasi Á, Lagzi I, Mészáros R (2014) Dispersion modeling of air pollutants in the atmosphere: a review. Central Eur J Geosci 6(3):257–278. https://doi.org/10.2478/s13533-012-0188-6

Liu H, Wang G, Zheng X (2019) Three-dimensional representation of large-scale structures based on observations in atmospheric surface layers. J Geophys Res Atmos 124(20):10753–10771. https://doi.org/10.1029/2019JD030733

Liu S, Liang XZ (2010) Observed diurnal cycle climatology of planetary boundary layer height. J Clim 23(21):5790–5809. https://doi.org/10.1175/2010JCLI3552.1

Lotfy ER, Harun Z (2018) Effect of atmospheric boundary layer stability on the inclination angle of turbulence coherent structures. Environ Fluid Mech 18(3):637–659. https://doi.org/10.1007/s10652-017-9558-4

Lotfy ER, Abbas AA, Zaki SA, Harun Z (2019) Characteristics of turbulent coherent structures in atmospheric flow under different shear-buoyancy conditions. Boundary-Layer Meteorol 173(1):115–141. https://doi.org/10.1007/s10546-019-00459-y

Lu CH, Fitzjarrald DR (1994) Seasonal and diurnal variations of coherent structures over a deciduous forest. Boundary-Layer Meteorol 69(1–2):43–69. https://doi.org/10.1007/BF00713294

Marusic I, Mathis R, Hutchins N (2010) Predictive model for wall-bounded turbulent flow. Science 329(5988):193–196. https://doi.org/10.1126/science.1188765

Metzger M, Holmes H (2008) Time scales in the unstable atmospheric surface layer. Boundary-Layer Meteorol 126(1):29–50. https://doi.org/10.1007/s10546-007-9219-0

Moeng CH, Sullivan PP (1994) A comparison of shear- and buoyancy-driven planetary boundary layer flows. J Atmos Sci 51(7):999–1022. https://doi.org/10.1175/1520-0469(1994)051<0999:ACOSAB>2.0.CO;2

Moin P (2009) Revisiting Taylor's hypothesis. J Fluid Mech 640:1–4

Monin AS, Obukhov AM (1959) Basic laws of turbulent mixing in the surface layer of the atmosphere. Tr Akad Nauk SSSR Geophiz Inst 24(151):163–187

Monty J, Hutchins N, Ng H, Marusic I, Chong M (2009) A comparison of turbulent pipe, channel and boundary layer flows. J Fluid Mech 632:431–442

Monty JP, Stewart JA, Williams RC, Chong M (2007) Large-scale features in turbulent pipe and channel flows. J Fluid Mech 589:147–156

Newsom R, Calhoun R, Ligon D, Allwine J (2008) Linearly organized turbulence structures observed over a suburban area by dual-Doppler Lidar. Boundary-Layer Meteorol 127(1):111–130. https://doi.org/10.1007/s10546-007-9243-0

Nilsson E, Lohou F, Lothon M, Pardyjak E, Mahrt L, Darbieu C (2016) Turbulence kinetic energy budget during the afternoon transition—Part 1: observed surface TKE budget and boundary layer description for 10 intensive observation period days. Atmos Chem Phys 16(14):8849–8872. https://doi.org/10.5194/acp-16-8849-2016

Park SB, Gentine P, Schneider K, Farge M (2016) Coherent structures in the boundary and cloud layers: role of updrafts, subsiding shells, and environmental subsidence. J Atmos Sci 73(4):1789–1814. https://doi.org/10.1175/JAS-D-15-0240.1

Paw KTU, Brunet Y, Collineau S, Shaw RH, Maitani T, Qui J, Hipps L (1992) On coherent structures in turbulence above and within agricultural plant canopies. Agric For Meteorol 61:55–68

Perret L, Patton EG (2021) Stability influences on interscale transport of turbulent kinetic energy and Reynolds shear stress in atmospheric boundary layers interacting with a tall vegetation canopy. J Fluid Mech 921:1–49. https://doi.org/10.1017/jfm.2021.453

Rautenberg A, Graf MS, Wildmann N, Platis A, Bange J (2018) Reviewing wind measurement approaches for fixed-wing unmanned aircraft. Atmosphere 9(11):422. https://doi.org/10.3390/atmos9110422

Robinson S (1991) Coherent motions in the turbulent boundary layer. Annu Rev Fluid Mech 23(1):601–639. https://doi.org/10.1146/annurev.fluid.23.1.601

Romps DM, Charn AB (2015) Sticky thermals: evidence for a dominant balance between buoyancy and drag in cloud updrafts. J Atmos Sci 72(8):2890–2901. https://doi.org/10.1175/JAS-D-15-0042.1

Sadani LK, Kulkarni JR (2001) A study of coherent structures in the atmospheric surface layer over short and tall grass. Boundary-Layer Meteorol 99(2):317–334. https://doi.org/10.1023/A:1018992529079

Salesky ST, Anderson W (2018) Buoyancy effects on large-scale motions in convective atmospheric boundary layers: implications for modulation of near-wall processes. J Fluid Mech 856:135–168. https://doi.org/10.1017/jfm.2018.711

Salesky ST, Chamecki M, Bou-Zeid E (2017) On the nature of the transition between roll and cellular organization in the convective boundary layer. Boundary-Layer Meteorol 163(1):41–68. https://doi.org/10.1007/s10546-016-0220-3

Segalini A, Alfredsson P (2012) Techniques for the eduction of coherent structures from flow measurements in the atmospheric boundary layer. Boundary-Layer Meteorol 143:433–450

Senocak I, Ackerman AS, Kirkpatrick MP, Mansour Stevens N DE (2007) Study of near-surface models for large-Eddy simulations of a neutrally stratified atmospheric boundary layer. Boundary-Layer Meteorol 124:405–424

Sikma M, Ouwersloot H, Pedruzo-Bagazgoitia X, van Heerwaarden C, Vilà-Guerau de Arellano J (2018) Interactions between vegetation, atmospheric turbulence and clouds under a wide range of background wind conditions. Agric For Meteorol 255:31–43. https://doi.org/10.1016/j.agrformet.2017.07.001

Su T, Li Z, Kahn R (2020) A new method to retrieve the diurnal variability of planetary boundary layer height from lidar under different thermodynamic stability conditions. Remote Sens Environ 237(November 2019):111519. https://doi.org/10.1016/j.rse.2019.111519

Takimoto H, Sato A, Barlow JF, Moriwaki R, Inagaki A, Onomura S, Kanda M (2011) Particle image velocimetry measurements of turbulent flow within outdoor and indoor urban Scale Models and flushing Motions in urban canopy Layers. Boundary-Layer Meteorol 140(2):295–314. https://doi.org/10.1007/s10546-011-9612-6

Thomas C, Foken T (2007) Organised motion in a tall spruce canopy: temporal scales, structure spacing and terrain effects. Boundary-Layer Meteorol 122(1):123–147. https://doi.org/10.1007/s10546-006-9087-z

Tomkins CD, Adrian RJ (2003) Spanwise structure and scale growth in turbulent boundary layers. J Fluid Mech 490:37–74

Tomkins CD, Adrian RJ (2005) Energetic spanwise modes in the logarithmic layer of a turbulent boundary layer. J Fluid Mech 545:141–162

Townsend AA (1976) The structure of turbulent shear flow. Cambridge University Press, Cambridge

Träumner K, Damian T, Stawiarski C, Wieser A (2015) Turbulent structures and coherence in the atmospheric surface layer. Boundary-Layer Meteorol 154(1):1–25. https://doi.org/10.1007/s10546-014-9967-6

Weckwerth TM, Wilson JW, Wakimoto RM, Crook NA (1997) Horizontal convective rolls: determining the environmental conditions supporting their existence and characteristics. Mon Weather Rev 125(4):505–526. https://doi.org/10.1175/1520-0493(1997)125<0505:HCRDTE>2.0.CO;2

Weckwerth TM, Horst TW, Wilson JW (1999) An observational study of the evolution of horizontal convective rolls. Mon Weather Rev 127(9):2160–2179. https://doi.org/10.1175/1520-0493(1999)127<2160:AOSOTE>2.0.CO;2

Wildmann N, Rau GA, Bange J (2015) Observations of the early morning boundary-layer transition with small remotely-piloted aircraft. Boundary-Layer Meteorol 157(3):345–373. https://doi.org/10.1007/s10546-015-0059-z

Willmarth W, Lu S (1972) Structure of the Reynolds stress near the wall. J Fluid Mech 55:65–92

Witte BM, Singler RF, Bailey SCC (2017) Development of an unmanned aerial vehicle for the measurement of turbulence in the atmospheric boundary layer. Atmosphere 8(12):195. https://doi.org/10.3390/atmos8100195

Wyngaard JC (2010) Turbulence in the atmosphere. Cambridge University Press, Cambridge. https://doi.org/10.1017/CBO9780511840524

Zhou S, Peng S, Wang M, Shen A, Liu Z (2018) The characteristics and contributing factors of air pollution in Nanjing: a case study based on an unmanned aerial vehicle experiment and multiple datasets. Atmosphere. https://doi.org/10.3390/atmos9090343